Study of Imaging Depth in Turbid Tissue with Two-Photon Microscopy

by

Benjamin Andreas Holfeld

Thesis

Presented to the Faculty of the Graduate School of

The University of Texas at Austin

in Partial Fulfillment

of the Requirements

for the Degree of

Master of Science in Applied Physics

The University of Texas at Austin

December 2007

Study of Imaging Depth in Turbid Tissue with Two-Photon Microscopy

Approved by
Supervising Committee:

Adela Ben-Yakar

Ernst-Ludwig Florin

Dedication

For my parents,

Thank you for your love and support.

Acknowledgements

First of all, I would like to thank my supervisor, Dr. Adela Ben-Yakar for providing generous funding to exciting research projects and for motivating discussions. Her ideas to use modern laser technology for medical applications fascinate me.

I am equally thankful to my fellow group members and friends Nicolas Durr and Dr. Frederic Bourgeois. Nick provided me with the knowledge to work in the lab and was always willing to answer my never ending questions. I remember many discussions which resulted in new ideas and concrete steps for further proceeding with the research. Frederic was always around and helped out whenever I had questions concerning lab and purchasing procedures.

For reviewing my thesis, I would like to thank Prof. Ernst-Ludwig Florin from the physics department. For support, motivation and help in finishing this thesis I would like to thank my family and my friends from Austin.

Finally I would like to thank all of the above and the remaining members of the group Chris Hoy, Daniel Eversole, Sam Guo, Priti Duggal and the new members Christian, Siegfried, Sheldon, Navid and Özgür for the great atmosphere in which I had the privilege to work.

Benjamin A. Holfeld

University of Texas at Austin

December 2007

December 7th 2007

Abstract

Study of Imaging Depth in Turbid Tissue with Two-Photon Microscopy

Benjamin Andreas Holfeld, M.S.Appl.Phy.

The University of Texas at Austin, 2007

Supervisor: Adela Ben-Yakar

Two-photon microscopy has the potential to detect cancerous cells in epithelial tissue. We designed and constructed a two-photon microscope and imaged cancer cells down to 200μm depth in highly scattering tissue phantoms. A decline of resolution was found to be negligible, while a strong increase in background fluorescence was detected.

We next performed a theoretical analysis to determine what parameters can be optimized to improve imaging depth. Investigations of the focused laser beam show out-of-focus fluorescence generation near the surface of the sample during deep imaging. Scattering is the factor which mostly leads to this background fluorescence in tissue. Thus the optimum excitation wavelength range for deep imaging in the epidermis is 1000 to 1400 nm, where scattering is minimal. A general study of the collection efficiency of light emission from fluorescence within turbid media reveals how scattering increases the collection efficiency and how absorption decreases it in depth. These simulations showed that the optimal emission wavelength range in epidermis would be between 800 to 1200 nm, where absorption is minimal. Promising contrast agents are gold nanorods as their excitation and emission maximum can be tuned to the desired wavelength ranges.

Contents

Glossary

Term	Definition
Acceptance Angle	The maximum angle under which a ray can enter and transmit through an optical part.
Back Aperture (BA)	The aperture of the objective lens which faces towards scanning and collection optics. The side opposite of the sample side.
Background Signal	Signal due to out-of-focus fluorescence emission.
Ballistic Light	Light that propagates without being scattered.
Collection Efficiency	The amount of collected fluorescence compared to the total fluorescence emitted from one point in the sample (e.g. from the focal point)
Contrast Agents	Fluorescent dye with special emission/excitation properties
Dichroic Mirror	A mirror which reflects light of a particular wavelength range and transmits another range.
Emission	Generated fluorescence
Field of View (FOV)	Observed area in the sample
Fluorophore	A fluorescent molecule, such as NADH or a fluorescent dye
Focal Spot	Focal point of the focused laser beam
Front Aperture (FA)	The side of the objective which faces towards the sample
Fundamental Imaging Depth Limit	The imaging depth at which the signal fluorescence is equal to the background fluorescence
Gold nanorods	Nanometer scale rods of gold used as a contrast agent for two-photon luminescence
Half-Wave-Plate (HWP)	Introduces a half wavelength of phase retardation to an optical field to rotate the polarization
Imaging Depth	Distance between focal point and sample surface

Intralipid	Substance with scattering particles: Used to prepare samples with optical parameters similar to tissue.
Inverted TPM	The sample lies above the objective of the microscope
Lossless media	Optical media without scattering or absorption
MaiTai	A modelocked Ti:Sapphire femtosecond pulsed laser oscillator from SpectraPhysics
Mean Free Path (MFP)	The average distance the photon travels between scattering or absorption events
Monte Carlo Simulation	Common method to study the propagation of light in a turbid media by propagating rays using random number generation
Multi Photon Scope	A software package used for data collection and image reconstruction developed by David Kleinfeld's group (UC San Diego) to control a Two-Photon Microscope.
NADH	A fluorescent coenzyme found naturally in living cells
NanoMax	A precise stepper motor from Thorlabs to move the probe
Near Infrared (NIR)	Wavelength range between ~700 nm and 1000 nm, with low scattering and absorption in tissue.
Numerical Aperture (NA)	A term representative of the angle defining the cone of light accepted by the objective of a microscope. $NA = n \cdot \sin(\theta)$
Objective lens	Focuses laser light and collects emitted fluorescence from sample
Out-of-Focus	The region of the sample outside the focal spot
Photomultiplier Tube (PMT)	Extremely sensitive detector of emission light
Polarizing Beam Splitter	An object that reflects light with a given polarization and transmits the orthogonal polarization
PSF	Point spread function – minimum resolution of an optical system

Sample Surface	The surface where the turbid media begins
Scanning Mirrors	Mirrors that scan the laser beam through an optical system to raster the focal point over the field of view
Scattering Anisotropy	Describes the angular distribution of scattered light
Signal	Fluorescence from focal spot
Signal to Background ratio (Sgn/Bkd)	Compares the fluorescence generation from the focal spot (signal) to the fluorescence generation from out-of-focus
Signal to Noise Ratio (SNR)	Noise is generated through external light, electrical noise and photon shot noise. While the first two can be diminished with an optimized setup, the shot noise is fundamental due to the quantization of photons. The SNR is the ratio of signal to the total amount of noise.
Spatial Uniformity	Describes how homogenous the scanned area is excited and detected. Focal spots at the outer margin of the field of view lead to less generation and collection. Thus the inhomogeneity decreases for a large FOV.
Spherical Aberration	The failure of a lens system to image the central and peripheral rays at the same focal point.
Tissue phantom	A 3D tissue-like structure made with cultured cells to be optically similar to natural tissue structures.
TPM	Two-photon microscopy or two-photon microscope
Turbid media	Sample or media with high scattering and absorption properties
Upright TPM	Two-Photon Microscope with the objective pointing downwards onto the sample (Necessary to use a water immersion objective)
Working Distance (WD)	The distance between the cover glass or object and the tip of the objective lens restricting the allowable movement of the objective lens

1 Introduction

In 2006, 1.4 million new cancer cases were diagnosed in the US, of which almost 600,000 will end in death [1]. Soon, cancer could be the most common cause of death in industrialized countries due to aging populations. Thus, there is a growing need for more effective methods to fight cancer. Conventional therapies attempt to target only cancerous cells but also harm healthy cells, resulting in undesired side effects. An ideal treatment with fewer side effects would be the precise removal of cancerous cells only. One promising technique for this goal is the visualization of cancer cells with laser scanning fluorescence microscopy, along with the precise destruction of these cells with pulsed lasers. Two-photon microscopy (TPM) has been proven to be an excellent technique to image deep into highly scattering tissue with high resolution [2], [3]. TPM can make use of near infrared excitation laser light which undergoes less attenuation in tissue, and non-linear two-photon excitation, which creates less background fluorescence than confocal microscopy, for maximal signal. Studies down to a depth of 40μm have been performed which show significant differences in the images of cancerous and healthy cells as cancerous cells produce significantly more of the fluorescent molecule NADH [4]. The major disadvantage of observing tissue with visible and near-infrared laser light is its limited tissue penetration depth in the range of a couple of millimeters compared with other radiation techniques as x-ray or proton radiation. The maximum imaging depth in turbid media using TPM is limited by out-of-focus fluorescence [5]. Depending on the optical properties of the sample, at a certain depth, TPM will produce more out-of-focus fluorescence than signal fluorescence from the focal point which makes imaging impossible.

Nevertheless, more than 85 % of all cancers begin in epithelial tissue [6] which is easier to probe with a two-photon endoscope. The epithelium, the outermost layer of the tissue, can be as thick as 500 μm. Demonstrating and improving deep imaging into epithelial tissue with TPM is thus an important step towards developing methods for precise detection and treatment of cancerous cells. Up to now imaging into human skin

tissue has been demonstrated 100 μm deep [7]. This is low compared to brain imaging, where imaging depths in the range of one millimeter have been achieved [29]. In recent years, several methods were discovered to increase imaging depth into highly scattering media. These are discussed in section 2.3.

The aim of this thesis is to experimentally and theoretically investigate the imaging depth limit in human tissue as a highly scattering medium with TPM, and to describe strategies for further imaging depth improvement. In Chapter 2, the TPM is described, characterized and suggestions are given to increase the collection efficiency of the setup. To study deep imaging performance, we measured resolutions for different imaging depths in a scattering sample. According to theoretical results presented in Chapter 3, the imaging depth was found to be limited by high background fluorescence. The signal-to-background ratio was measured, and a deeper penetration was found for higher excitation wavelengths. Cancerous tissue phantoms were imaged and compared with gold nanorod labeled cancerous cell phantoms.

The second part of Chapter 3 includes theoretical investigations of background fluorescence generation and collection. Calculations show that during deep imaging, fluorescence is created in an ellipsoidal volume close to the surface which is measured as background noise. The propagation of light from sources within the turbid medium as well as the collection through an objective lens was investigated using Monte Carlo simulations. These simulations show that scattering improves collection from near-surface fluorescence while absorption deteriorates the collection efficiency. Moreover, we explain how contrast agents such as gold nanorods can help to improve the imaging depth.

2 The Two-Photon Microscope for Deep Imaging

This chapter describes the design, construction and characterization of a Two-Photon Microscope for deep imaging in turbid media. After a short introduction into the underlying physical process of two-photon excitation, the general setup of the microscope will be described. Next, the known factors limiting the imaging depth are listed. Based on these factors, the particular design for deep imaging is documented. The accuracy of the scanning stage, the resolution and the image quality are characterized. The last section of this chapter shows how the collection efficiency can be improved by collecting more scattered angles.

2.1 Two-Photon Excitation

TPM is based on two-photon excitation which was predicted theoretically by Göppert-Mayer in 1931 [8]. In 1961, two-photon excitation was first experimentally observed [9], and with the further development of pulsed high energy lasers and modern computer technology, its application for microscopy was demonstrated in 1990 [10]. Two or Multi-photon excitation is a nonlinear optical process which requires the absorption of two or more photons by atoms or molecules within a very narrow temporal window, typically less than 10^{-15} s as defined by the Heisenberg uncertainty principle. The excited molecule will then pass through different vibrational states and emit a photon with approximately n times the energy of each individual photon, where n is the number of photons absorbed. Because of non-radiative energy loss in vibrational states, multiphoton excited molecules can emit over a broad range (See Figure 1a and Figure 29). The fluorescent molecules are called fluorophores.

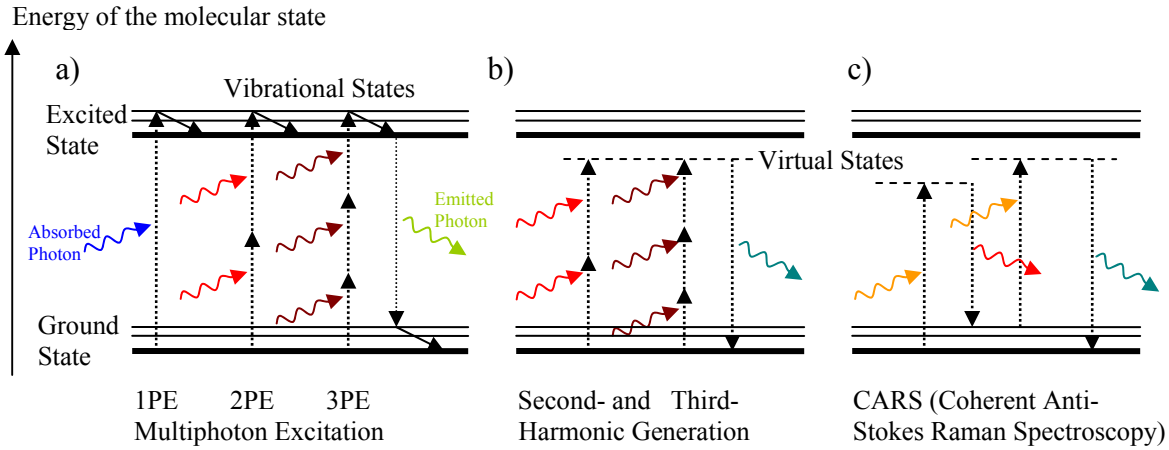

Figure 1: Comparison of Two Photon Excitation (TPE or 2PE) to other nonlinear optical processes in molecules, which are used in fluorescence microscopy.

In contrast to TPE, during harmonic generation, only photons with *n* times the energy of the absorbed photons will be emitted. Multi-photon fluorescence is emitted isotropically, while harmonic generation and CARS emission is mostly forward directed.

Unlike one-photon absorption, two photon absorption scales with the square of the intensity and significant two-photon absorption rates require very high photon flux densities in the range of GW/cm^2. These can be achieved by temporal and spatial concentration of laser light. Although two-photon excitation was observed using only spatial confinement, temporal concentration through pulsed radiation is necessary to generate images time efficient and with acceptable laser power. A focused pulsed laser beam creates very high laser intensities at the focal volume which leads to two-photon excitation at fluorescent molecules. A photon pair which is absorbed by such a fluorescent molecule, excites the molecule to a higher vibrational state. The fluorescence emission from the focal spot which is later called signal, is proportional to the amount of absorbed photon pairs. The average number of photon pairs absorbed while focused into a fluorophore is given per unit time according to [10] by:

$$n_{absorbed} = \frac{\delta}{\tau \cdot f}\left(\frac{\pi(NA)^2}{hc\lambda}\right)^2 \langle P \rangle^2 \tag{2.1a}$$

With two-photon absorption cross-section δ, laser repetition rate f, laser pulse duration τ, laser wavelength λ, average power $\langle P \rangle$, numerical aperture of the objective (NA), Planck's constant h, and speed of light c.

Increasing the number of absorbed photon pairs and thus the fluorescence generation from the focal spot improves the ratio of signal to background and thus the imaging depth as explained in section 2.3.

2.2 The Two-Photon Microscope in General

In contrast to a normal bright-field or fluorescence microscope, a two-photon microscope (TPM) scans the sample point by point and collects the resulting fluorescent light of each point with a detector, which is typically a photomultiplier tube (PMT). The acquired data can be reconstructed to a three dimensional high-resolution image via data processing technology. The architecture is similar to a confocal laser scanning microscope but has the advantage that no detector aperture, which filters out-of-focus light. In TPM, fluorescence is mostly generated at the focal spot, due to the square dependence of the fluorescence on the excitation intensity. Thus, in contrast to confocal laser scanning microscopy, scattered light can also be detected. This improves the collection efficiency in depth significantly as emitted light from deep within tissue will be mostly scattered. The complete setup which was designed for deep imaging is shown in Figure 2 and Figure 3. The basic components are a near-infrared ultra-short pulse laser as the excitation light source, scanning mirrors and optics to raster the focal point through the sample behind the objective, and a detector to collect the fluorescent photons. Some advantages for deep imaging are already noticeable in this schematic: The upright architecture allows the use of a water immersion objective to minimize refraction mismatch with the sample and the black box absorbs surrounding light to minimize background noise which could enter the PMT and decrease the Signal-to-Noise ratio.

2.3 Limits for the Imaging Depth

Imaging depth with Two Photon Microscopy is limited by the fluorophores sample, the laser excitation, and the collection efficiency [11]. While in the past the achievable laser power was a limiting factor, today we encounter a new fundamental imaging limit at a depth where the high laser power needed for deep imaging, generates as much out-of-focus fluorescence as fluorescence from the focal spot [5]. In the following sections, the limiting factors are listed with strategies for improvement in deep imaging, based on published data and calculations.

2.3.1 Sample

Optical properties of the sample such as scattering, absorption, refraction, staining inhomogeneity, and maximum tolerable intensities are limiting factors. Knowing these parameters, imaging depth can be improved by several methods. First, the sample can be stained with a contrast agent that can be excited at a wavelength with minimal absorption and scattering. This approach is analyzed in section 3.4. Second, an objective with matching refractive index to minimize aberration should be chosen, as a mismatch causes spread of the radial and axial resolution in depth [12]. Finally, the use of clearing agents to reduce scattering [13] as well as inhomogeneous or targeted staining [5] has been shown to increase imaging depth. For medical applications it is also necessary to consider maximal tolerable irradiation intensity, as TPM shows highly nonlinear photodamage [14], [15] which can lead to degradation of the examined sample.

2.3.2 Excitation

It has been shown theoretically and experimentally that a short pulse duration [16], low repetition rate [17], and high NA increase the penetration depth of turbid media[5] due to higher fluorescence generation at the focal spot (See Equation 2.1a). Laser pulse duration down to 15fs [18] and repetition rates of 4 MHz [19] have been achieved by pre-chirping and cavity dumping. A threefold increase in imaging depth was observed using a 40fs

instead of a 250 fs laser pulse [16] as well as deeper imaging of 2-3 scattering mean free path at lower repetition rates [17]. However, decreasing the pulse length to less than 25 fs begins to appreciably spread its spectral width and therefore lowers the excitation efficiency of the fluorophore. Considering medical applications, a decrease of the repetition rate below 1MHz, while keeping the same average power, is not desirable as the total image acquisition time will become too long. Finally, overfilling the objectives back aperture will decrease the size of the focal spot, which is equivalent to a larger NA and thus slightly improves the imaging depth, as well as the resolution.

2.3.3 Collection

The signal to background ratio depends strongly on the collection efficiency of emitted light from the focal spot. Emission light from deep within turbid media will often be scattered multiple times before leaving the sample surface and possible collection from the objective. This process is examined in detail in section 3.5. This section shows that scattering helps to deliver more light to the objective as photons that first traveled into the opposite direction may be backscattered. Moreover it is shown that absorption is the main limiting factor for collection from deep within tissue. Photons coming from deep within turbid media will be multiple scattered and enter the objective front aperture at steeper angles. Hence it is important to have a large acceptance angle, and a large front aperture of the objective to collect a large part of the emitted fluorescence. This is achieved with high NA, low magnification and a large field-of-view objective. Additionally, blocking of out-of-focus background signal in the collection path can improve the signal-to-background ratio (at the expense of reduced signal) and improve the imaging depth around half a scattering length [5].

2.3.4 Definition of the Imaging Depth Limit

There are different definitions for the imaging depth limit. It is important to understand the differences in order to compare values. A definition introduced by Mertz et al. [20]

was, to assume a minimum fluorescence at the focal spot n_{min}, which corresponds to a minimum power P_{min} using Eq. 2.1a. Assuming an exponential attenuation of laser light due to the scattering mean free path l_s: $\langle P_{\min} \rangle = \langle P_0 \rangle e^{-z_{\max}/l_s}$, the maximum imaging depth is given by:

$$z_{\max} = l_s \ln\left(\frac{\pi \cdot (NA)^2}{hc\lambda} \langle P_0 \rangle \sqrt{\frac{\delta}{n_{\min} \cdot \tau \cdot f}} \right) \tag{2.3a}$$

According to Equation 2.3a, the imaging depth can be increased to any depth just by increasing power and NA and by lowering pulse duration, wavelength, and repetition rate. But experiments and calculations show a strong background signal which does not allow imaging below a certain depth. A more realistic definition for the fundamental depth limit introduced by Theer and Denk 2006 is the depth at which [5]:

$$Fluorescence_{OutOfFocus} = Fluorescence_{FocalSpot} \tag{2.3b}$$

The calculation of this imaging depth cannot be done using an analytical solution in most cases as the fluorescence needs to be calculated by integrating the square of all ballistic and scattered light over the fluorophore distribution. At this depth, the signal can still be distinguished from the background on the image as the signal will be overlaid with background. However, this definition does not consider the losses in collection efficiency due to depth, which are inevitable in turbid media as will be shown in section 3.5. The consequences of Theer and Denk's definition of the depth limit and the depth-dependency of the collection efficiency are demonstrated later in this chapter in numerical calculations and simulations.

For the use of TPM for cancer detection, it might be useful to define an imaging depth limit where healthy cells still can be distinguished accurately from cancerous cells.

2.4 Design and construction

Considering about the depth-limiting factors discussed in section 2.3, a two photon microscopy setup was designed and constructed for deep tissue imaging.

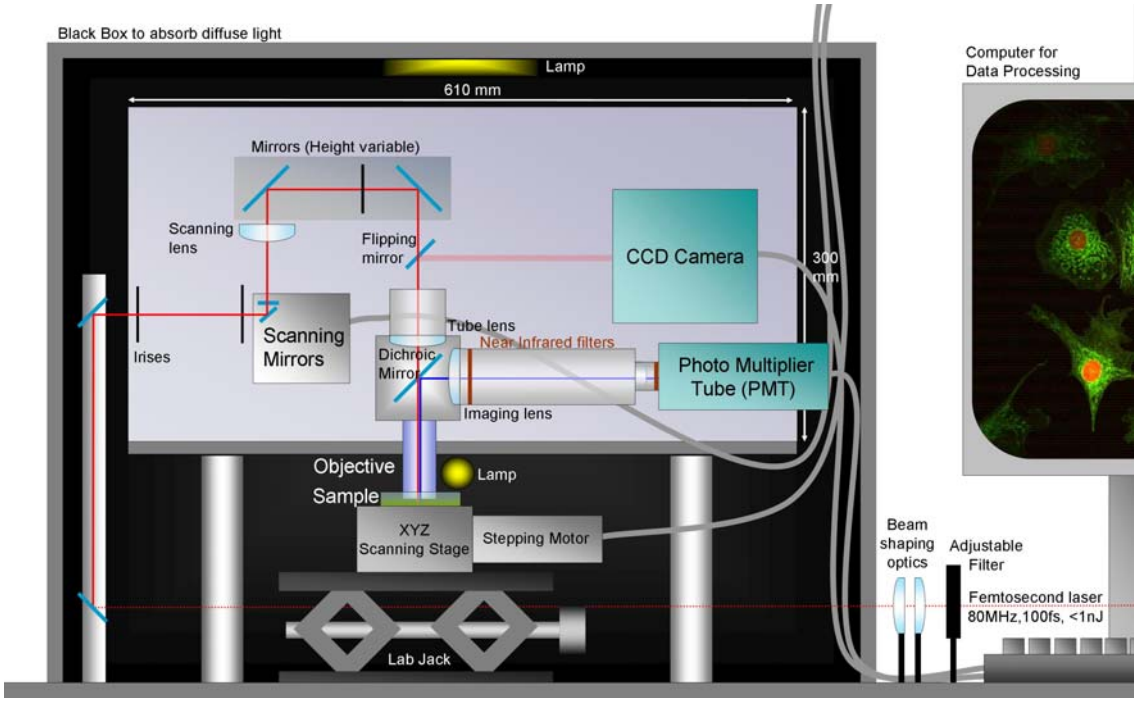

Figure 2: **Schematic of the home-built upright two-photon microscope**

Figure 3: Photograph of the home-built upright two photon microscope

2.4.1 Excitation Light Source

Peak intensities in the range of GW/cm^2 for two-photon-excitation are achieved with focused femtosecond laser pulses. Light sources that have been used in two-photon microscopy include solid-state lasers such as Nd:YLF, Nd:Glass, Cr:LiSAF, and Cr:Fosterite, as well as fiber and dye-based lasers [21]. The most commonly used light source, however, is the Ti:Sapphire mode-locked laser, due to its high average power capability up to 3 W, broad tuning range from 700 - 1100 nm, short pulse duration (less than 100 fs) as well as reliable and robust operation. For the TPM discussed in this thesis, a Ti:Sapphire laser ("MaiTai" from SpectraPhysics) was used with a tunable wavelength from 710 to 920 nm, a spectral pulse FWHM ~ 8 nm, and temporal FWHM of approximately 100 fs. While the pulse travels through filters and lenses, the pulse spreads (chirps) in time due to the different frequency phase velocities in the medium (group velocity dispersion). We measured 150 fs after a telescope, and at the focal point of the new TPM we estimated a pulse width of 400 fs due to the additional lens systems. This effect can be avoided by pre-chirping the pulse.

The lateral intensity distribution of the beam was measured using a Beam Analyzer (LBA-7XXPC, Spiricon) and was verified with the common knife edge method. At the distance for the new TPM, the laser produced a rather elliptical shape. (Using cylindrical lenses, the intensity distribution can be reshaped to a circular distribution (Figure 4)). However, as the back aperture of the objective is overfilled by the beam, the cylindrical lenses do not significantly improve the imaging quality.

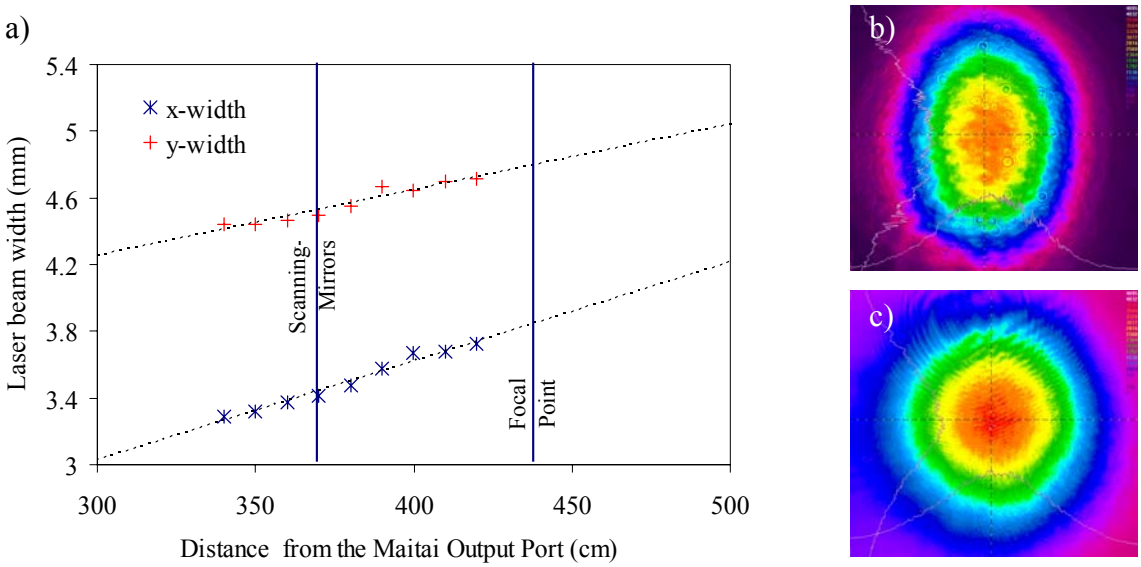

Figure 4: (a) The $1/e^2$ laser beam width and height from MaiTai at different distances measured with the Beam Analyzer. The beam profile several meters away from the output port behind a beam expander changes with distance and is elliptical at the focal point of the TPM (b). Cylindrical lenses with f_1 = -100 mm and f_2 = 80 mm can be used to create a circular shape at the position of the focal point.

2.4.2 Power attenuation

For imaging, the power needs to be increased from tens of µW to several mW. As high energy pulsed lasers cause nonlinear effects in common absorbing or reflecting filters, the power needs to be attenuated by using a half-wave plate and a beam splitter. The laser power can be adjusted in a specific range by turning the HWP from 0° to 45°. As the measurement in Figure 5 shows, this range varies with wavelength for the 808nm half-wave-plate (HWP) used in this TPM.

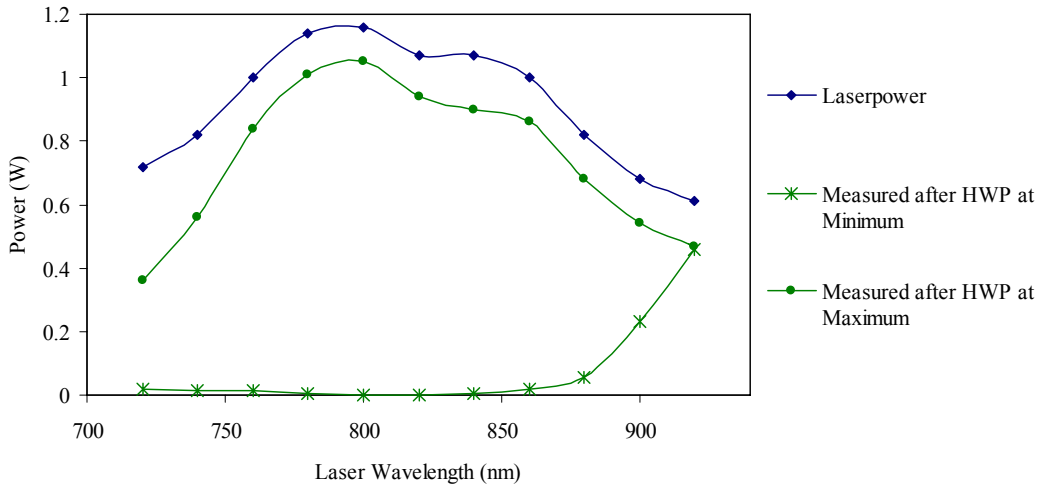

Figure 5: Laser power of the Ti:Sa – Laser as displayed by the MaiTai software (blue line) and the measured maximum, minimum adjustable power using a 808 nm half-wave-plate (HWP) and a beam splitter.

After the light passed through lenses, coatings, and the objective lens, the laser power at the sample was measured to be 38 ± 5 % of the incident power.

2.4.3 Objective Lens

Considering the factors that influence imaging depth, an objective with high NA, low magnification, and high field of view is necessary in order to increase the fluorescence generation as well as the collection efficiency (See section 2.3). Furthermore, the immersion fluid should have a similar refractive index to the sample to avoid aberrations and spread of the focal point. The average refractive index of all tissue is approximately 1.4 (See section 3.2 and [22]) and therefore using a water immersion objective is usually the best choice. The use of a water immersion lens requires the design of an upright system as water immersion objectives are difficult to handle in inverted setups. Moreover, the working distance should be greater than 1mm in order to demonstrate deep scanning in different scattering environments. Finally, we chose an Olympus 20x, 0.95NA objective lens with a 2 mm working distance, and a back aperture (BA) of

17 mm (See Figure 6). In order to overfill this large back aperture and to collect all the emitted light, special lens systems are necessary as described in the next sections.

Compared to other objectives with larger NA (Zeiss C-Apo LDC, and Nikon CFI W Plan), the focal spot is larger – but it has been shown that an objective with low magnification improves deep imaging in turbid media [20].

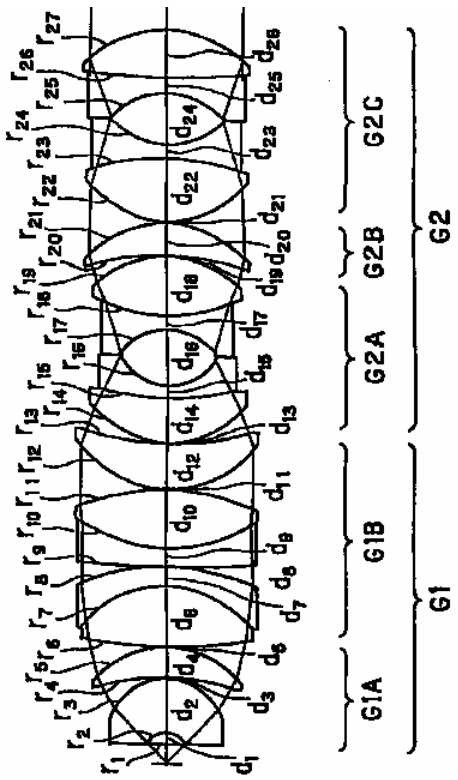

#	R	D	N_d	υ_d
1	∞	1.6100	1.45853	67.94
2	−2.4060	5.7597	1.75500	52.32
3	−6.5059	0.2000		
4	−25.5003	3.1500	1.49700	81.08
5	−10.9323	0.1200		
6	56.1096	6.4800	1.49700	81.08
7	−11.9889	1.9500	1.52944	51.72
8	−25.3665	0.1200		
9	223.7456	1.9500	1.75500	52.32
10	17.0397	6.5000	1.43875	94.99
11	−25.4913	0.1200		
12	12.1419	4.8264	1.43875	94.99
13	30.1344	0.2000		
14	10.8233	4.7695	1.43875	94.99
15	26.5356	1.5024	1.59551	39.21
16	6.2707	6.1162		
17	−6.9886	1.5000	1.61340	43.84
18	18.1665	6.3698	1.43875	94.99
19	−11.5665	0.2500		
20	−26.3050	3.3649	1.49700	81.08
21	−11.8757	0.1200		
22	10.9414	7.0500	1.43875	94.99
23	−25.6275	1.6500	1.52944	51.72
24	8.8733	5.6500		
25	−8.4093	1.7500	1.51633	64.14
26	95.8203	5.1500	1.61293	36.99
27	−12.3982			

β = −20X NA = 0.94 F = 9.006 mm WD = 2.04 mm

Condition (1) value:	D/F	=	8.914
Condition (4) value:	$\lvert \upsilon_{dpe} - \upsilon_{dne} \rvert$	=	27.15
Condition (5) value:	$\lvert \upsilon_{dpi} - \upsilon_{dni} \rvert$	=	43.27 – 55.78
Condition (6) value:	r_a/r_p	=	0.369
Condition (7) value:	F/F_{g2a}	=	−0.609
Condition (8) value:	F/F_{g2c}	=	−0.043

Figure 6: Patent for the Olympus Objective used for deep TPM (Xlumplf 20x 0.95NA) – US Patent 12/31/2002. Patent No.: US 6,501.603 B2

2.4.4 Scanning Mirrors and Optics

To scan the focal point in two dimensions through the sample, the angle of incidence of the collimated laser beam on the objective's back aperture (BA) must be scanned. The variation of this angle is achieved by imaging the middle of the pivot points of the scanning mirrors on the center of the BA. For using the full NA, the imaging lenses are chosen to overfill the BA which are, in this case, $f_1 = 60$ mm and $f_2 = 250$ mm. This lens pair increases the beam width by 4.17 filling the BA with a factor slightly above 1. The

distance between the lenses must be fixed at $f_1 + f_2 = 310$ mm to create a collimated beam directed towards the BA. The distance from the pivot point to the first lens is calculated at 70.7 mm due to the fixed distance of the tube lens and the objective (Figure 7). The large magnification is necessary due to the small scan mirror diameter (6 mm). This means that the distance between the pivot points becomes four times larger in the image, causing a slight movement of the collimated beam on the BA. This decreases the image uniformity and depending on the objectives position, the image area is more uniform in one than in the other direction. (See section 2.5.4)

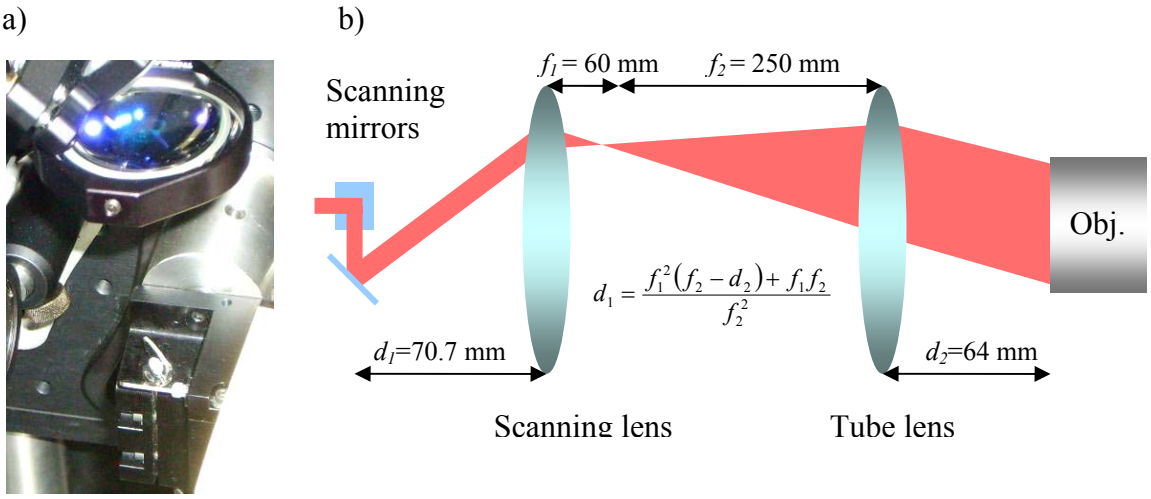

Figure 7: **(a) Scanning mirrors from Cambridge Technologies (Boston, MA) with scanning lens mounted above. (b) A sketch of the scanning optics including distances and imaging equation.**

2.4.5 Collection Optics

In order to gain a high signal from the focal spot, it is necessary to collect as many emitted photons as possible. In a medium without scattering or absorption, the 20x-Olympus objective's front aperture (FA, Diameter = 4 mm) covers 15 % of the emission sphere from the focal spot at a 2 mm working distance. Emission light from the focal spot at a maximum radial offset $x_{max} = 170$ µm and the focal width of the objective lens $f = 9$ mm, exits the back aperture parallel with an angle to the optical axis $\tan^{-1}(x_{max}/f) \approx 1°$. However, depending on the imaging depth, most of the emission light gets scattered, absorbed and will enter the objective under different angles than rays from the focal spot.

The scattered photons can then exit the back aperture under larger angles than photons from the focal spot. Due to the NA of 0.95, the objective used can collect rays which enter the objective as steep as 45°. Experiments showed that light can exit the back aperture under angles as large as 60°, depending on the ray's origin. To increase the collection of emission light, also rays which exit the BA under steep angles need to be accepted, which means to increase the acceptance angle of the collection optics. The first part in the collection path is a dichroic mirror which reflects the emission light into the PMT and prevents reflection of laser light into the PMT. We use a dichroic mirror (FM203, Thorlabs) with a diameter of 2" which is large enough to reflect all the angles which can be accepted by the PMT (See section 2.7). A displacement by Δx will assure to reflect light in all directions with the largest possible angle. (See Figure 8 and Equation 2.4a-b)

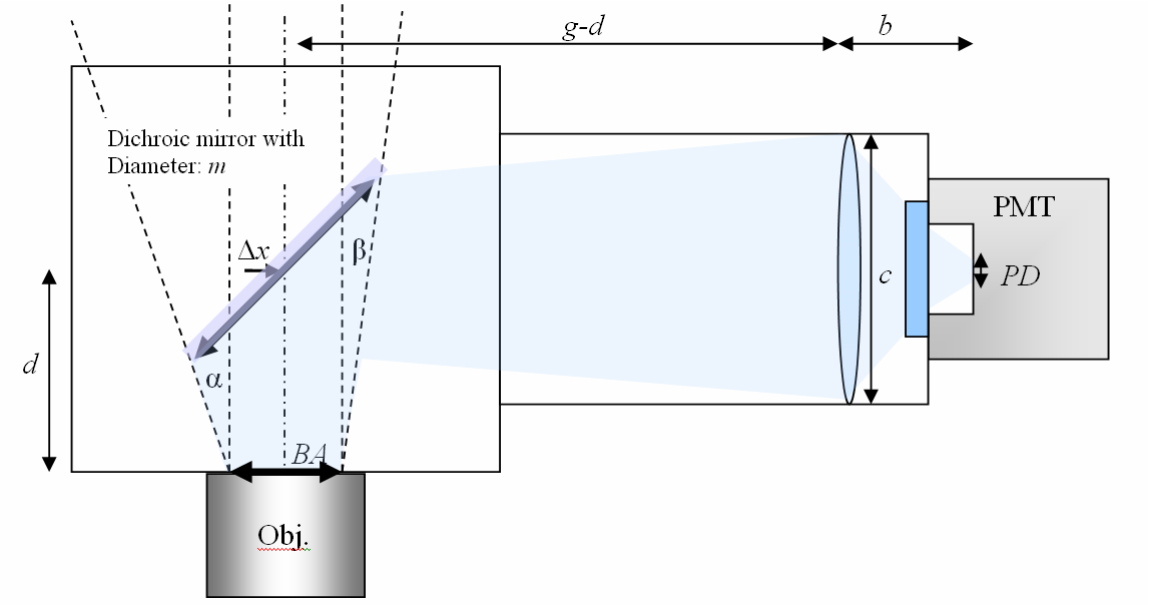

Parameters in the current setup:

BA: Back aperture = 17 mm *PD:* PMT cathode diameter = 4 mm s Lens diameter= 50.8 mm
g: Object distance = 225 mm *b:* Image distance = 53 mm *f:* focal length = 43 mm
m: Mirror diameter = 50.8 mm *d:* Distance BA-middle of mirror = 38 mm
α, *β:* Acceptance angles from outermost margins = 14° ,with Δx = 4.5 mm

Figure 8: Calculation of the acceptance angle from the dichroic mirror for rays from the outermost margin of the objective's *BA*. To accept the same angle in all directions, the mirror needs to be displaced by Δ*x*.

$$\beta = \tan^{-1}\left(\frac{\frac{m}{\sqrt{8}} + \Delta x - \frac{BA}{2}}{d + \frac{m}{\sqrt{8}}}\right) \quad \alpha = \tan^{-1}\left(\frac{\frac{m}{\sqrt{8}} - \Delta x - \frac{BA}{2}}{d - \frac{m}{\sqrt{8}}}\right) \tag{2.4a}$$

$$\Delta x_{\alpha=\beta} = \frac{m}{\sqrt{8} \cdot d}\left(\frac{m}{\sqrt{8}} - \frac{BA}{2}\right) \tag{2.4b}$$

Using the dimensions given in our particular setup with optimum displacement Δx = 4.5 mm, the full acceptance angle of the dichroic mirror α = β = 14°. A 3" mirror will increase this full acceptance angle to 26°.

The best collection of light with the PMT can be achieved by imaging the whole back aperture of the objective on the cathode of the PMT. The PMT used in this setup (H7422-40, Hamamatsu) has a 5mm cathode. We use a collection lens with a focal width of 43mm to reach a demagnification of 4. Using the imaging equation for lenses 2.4c, the distance from BA to the lens (g) is 225 mm and the distance from the lens to the PMT cathode (b) is 53 mm.

$$g = \frac{(BA + PD)}{PD} \cdot f \qquad b = \frac{(BA + PD)}{BA} \cdot f \tag{2.4c}$$

This design restricts the accepted angles to ± 5° which can only be improved with a larger PMT cathode as the calculations in section 2.7.2 show.

The collection efficiency is also decreased due to absorption of light in the objective, the dichroic mirror, the collection lens and filter. The transmission curves of the optics used are displayed in Figure 9. To avoid environmental light and noise, which decrease the imaging quality substantially, a black cover box was built to enclose the whole setup (See Figure 3). Finally, the sensitivity and quantum efficiency of the PMT itself strongly affects the final collection efficiency. For every pixel the collected signal is amplified and processed by a central computing unit.

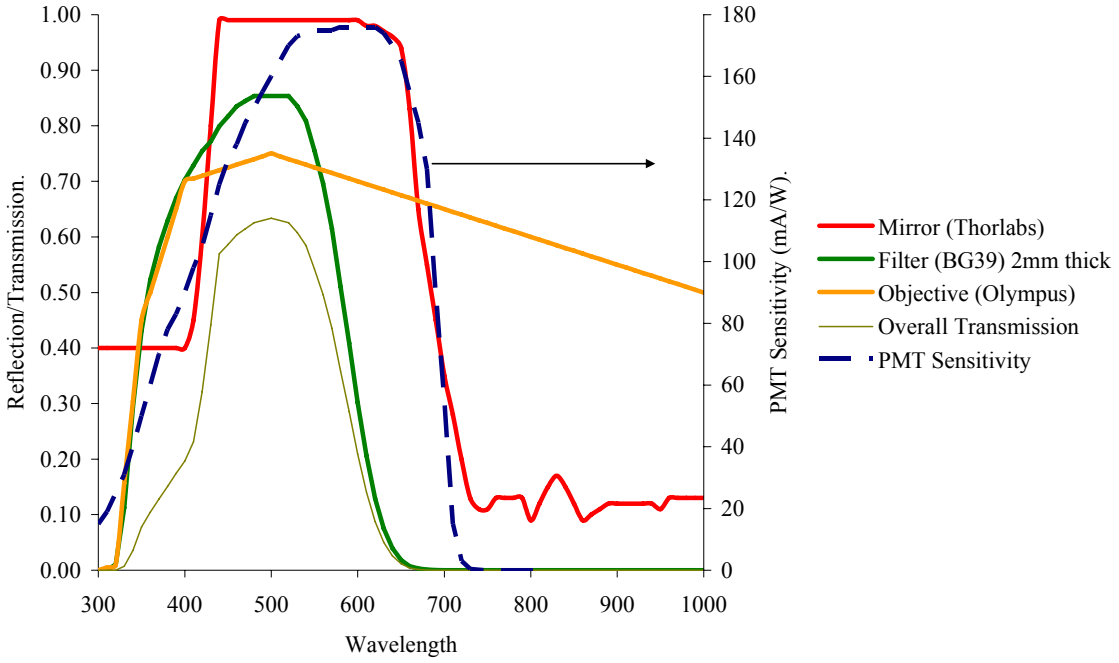

Figure 9: Transmission and reflection curves of objective, filter, dichroic mirror and the overall transmission through the collection path depending on the wavelength. The blue dashed line marks the Sensitivity of the Hamamatsu H7422-40 PMT.

2.4.6 Sample Scanning Stage

To scan the sample in z - direction and also move the field of view in *x* - and *y* - directions, we chose the 3-axis NanoMax Stepper Motors with 4mm travel and 25 nm resolution in each direction. The computer-controlled stage allows velocities from 1 - 2.5 mm/s with 1mm/s^2 accelerations.

Exact measurements with a calibration slide show that after 1mm travel, the real position deviates by 10 - 40 µm, introducing a relative error of 1-4 % in distance measurements with the NanoMax.

a) b)

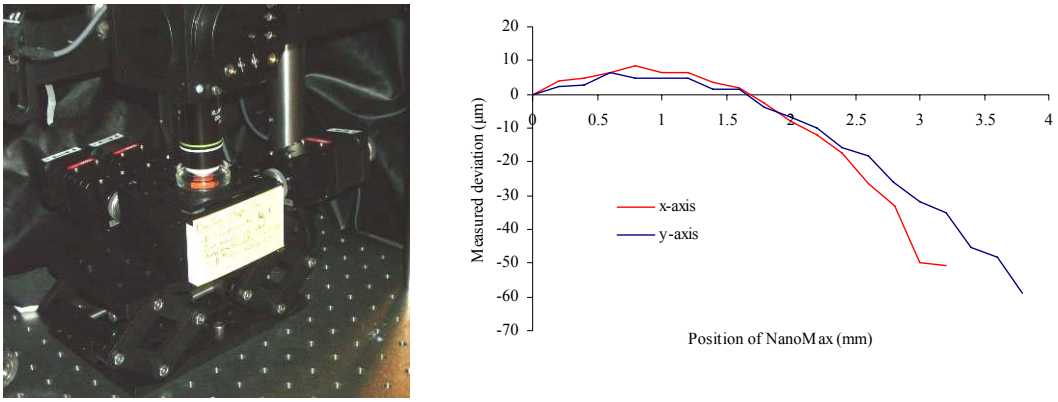

Figure 10: **(a) Photograph of the NanoMax Stepper Motors. (b) Difference between programmed distance beginning at 0 mm and the real distance, measured using a 50 µm grid.**

2.4.7 Controlling Software

The amount of scanned data acquired during TPM can only be managed using a central computing unit which consolidates the data to an image. An available software package to control the setup and manage the data is the Multi-Photon Scope (MP Scope) [23] which was developed by Dr. Kleinfeld's group in Borland Delphi for academic purposes. It enables the acquisition and analysis of multi-photon data using the programs MPScan and MPView, respectively. In order to use MPScan for the new TPM, the NanoMax stepper motor, an automated power control, and other features were added to the program source code (see Figure 12)

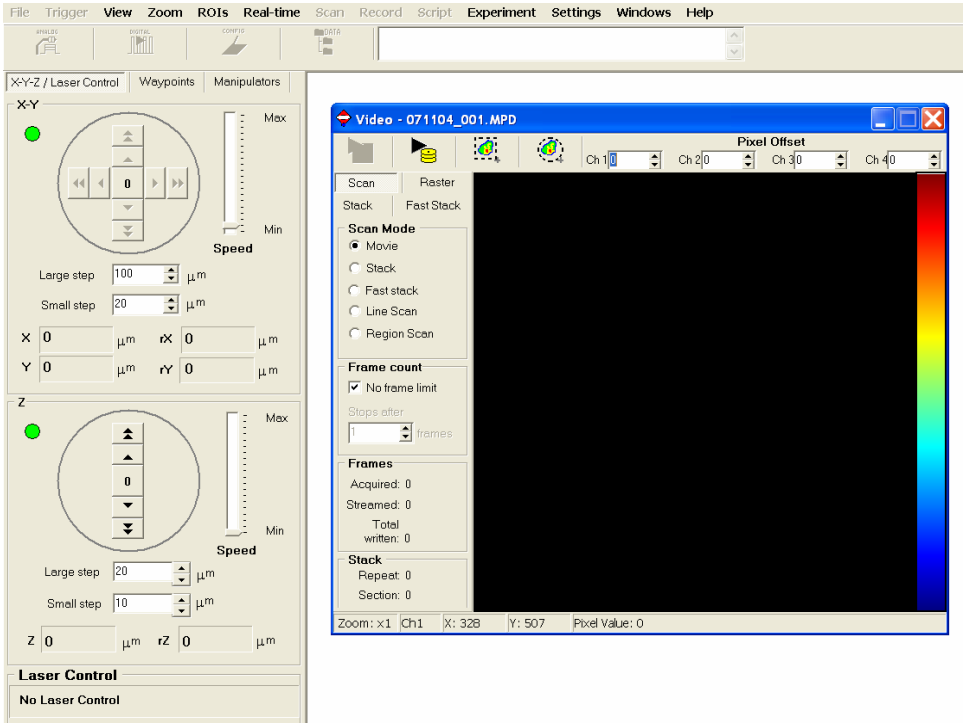

Figure 11: The original MPScan graphical user interface.

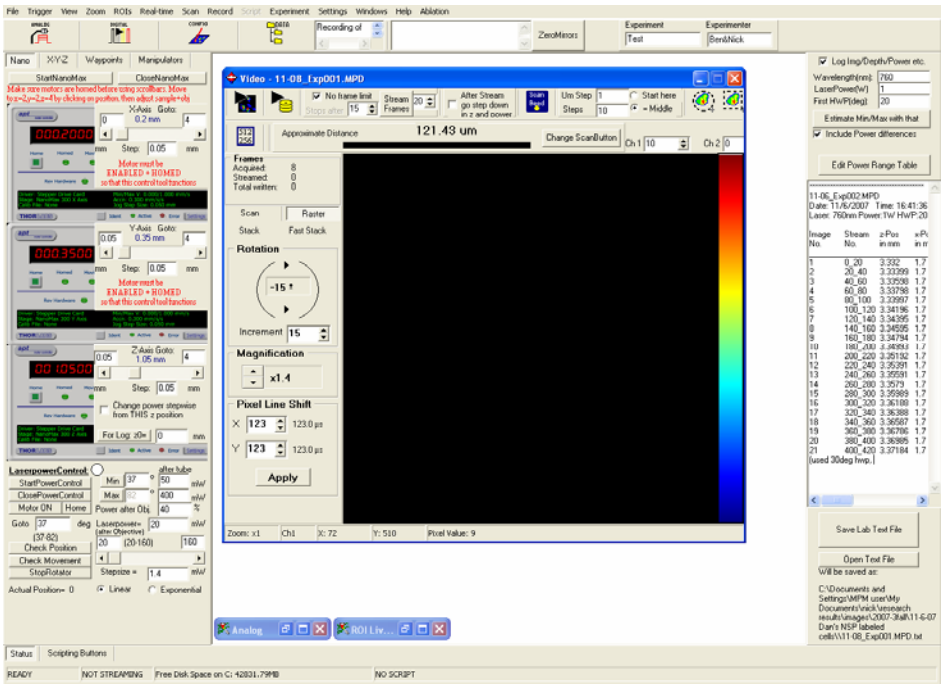

Figure 12: The modified version of MPScan for the new TPM with an adapted graphical user interface to control Nanomax and the laser power via rotating half-wave plate. In addition to that, automatic averaging, logging of scan data, scale bar, and an ablation tool were added.

The company Thorlabs delivers an AxtiveX-control with the NanoMax Stepper Motors which allows us to implement control and data of the NanoMax into any source code.

For automatic laser power regulation, we use a rotation stage from Newport that rotates a half wave plate (HWP) with an accuracy of 0.1°. The laser power can be accurately controlled by changing the polarization with the HWP and transmitting the laser through a beam splitter. To implement this stage into MPScan, the Newport software has to run in the background and is controlled via virtual key methods. The MPScan user must simply enter the desired laser power and, depending on the measured power range (See 2.4.1), the software calculates the angle of the HWP, by using Equation 2.4d.

$$\alpha = ArcSin\left(\frac{Power - b}{a}\right)\frac{45^{\circ}}{\pi} + \beta \qquad (2.4d)$$

where, a, b and β are constants that can be obtained out of power transmission measurements with the half wave plates. Notice that the constants a and b depend on the used wavelength and the angle of the manual HWP.

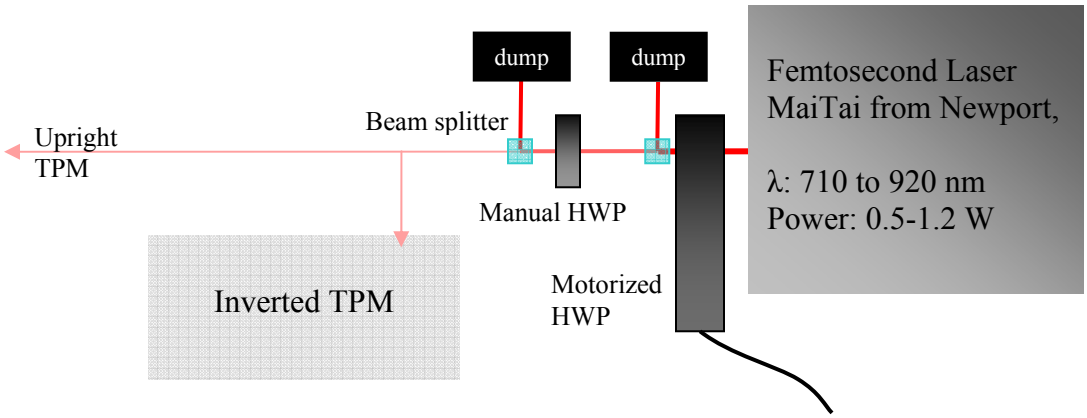

Figure 13: Arrangement of laser, motorized HWP and manual HWP on the optical table

The software can control complete depth scans automatically by increasing the power exponentially with depth. However, scanning of a cube with a 340 µm edge length can take up to an hour due to the mirror and amplifier's limited minimum pixel dwell time,

slow movement of the rotator, and required averaging of around 20 images per slide to increase the image quality.

The acquired data is stored in a format that can be edited using MPView and exported into multi-page Tiff files. Further image analysis and enhancement is performed with the public domain, Java-based image processing program ImageJ, developed at the National Institutes of Health.

2.5 Characterization

Characterizing the performance of the constructed setup and comparing it with theoretical calculations is important in order to understand and improve the imaging process in the home-built microscope. We measured the resolution, field of view, and field uniformity.

2.5.1 The First Image

After assembling the entire two-photon microscope, we were able to image a prepared slide from Molecular Probes which shows labeled bovine pulmonary artery endothelial cells. Figure 14 shows our first two-photon image indicating the nucleus (yellow) obtained at an excitation wavelength of 780 nm and cytoskeleton (green) obtained at 850 nm.

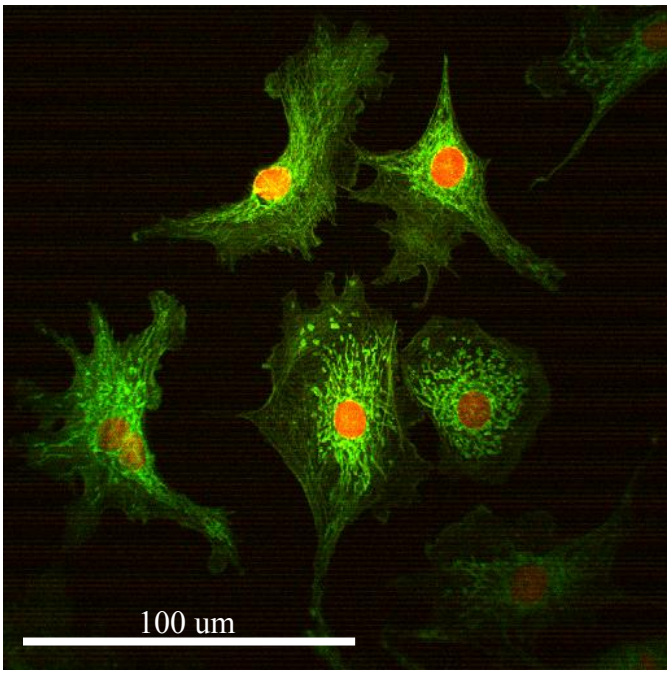

Figure 14: FluoCells® prepared slide #1: First image of a fixed sample of endothelial cells with the new TPM. At two different laser wavelengths (780 nm and 850 nm), 20 images were recorded at a rate of 3 frames per second and averaged. The resulting emission maps are overlaid in this figure with false colors.

This first image indicated that improvements in uniformity of the field of view and noise reduction are necessary. The noise was later reduced by isolating the whole setup from external light as well as disconnecting the cables that introduced noise signal to the amplifier.

2.5.2 Resolution

The resolution of a two-photon microscope depends on the size of the focal spot of the laser. The size of the focal spot can be measured by performing a 3D scan of a fluorescent bead which is much smaller than the focal spot. The intensity profile displays the convolution of the laser intensity with the bead, which can be assumed as a delta function because of its small size compared to the focal spot. Thus, the measured intensity profile, called the point spread function (PSF), is the focal spot, and its full-

width-half-maximum (FWHM) in *x*-, *y*- and *z*- direction corresponds to the radial and axial resolution, respectively. Any object which is examined with this microscope will be seen as the convolution of the PSF with this object.

For PSF measurements we use 100 nm fluorescent beads (FluoSpheres® F8803, Molecular Probes), which are yellow-green fluorescent carboxylate modified microspheres. The laser excitation wavelength is 920 nm. Gaussian-fitting the radial and axial PSF and averaging over 10-15 measurements result in a radial FWHM of 550 nm and an axial FWHM of 2300 nm, with an estimated measurement error of 10 % each.

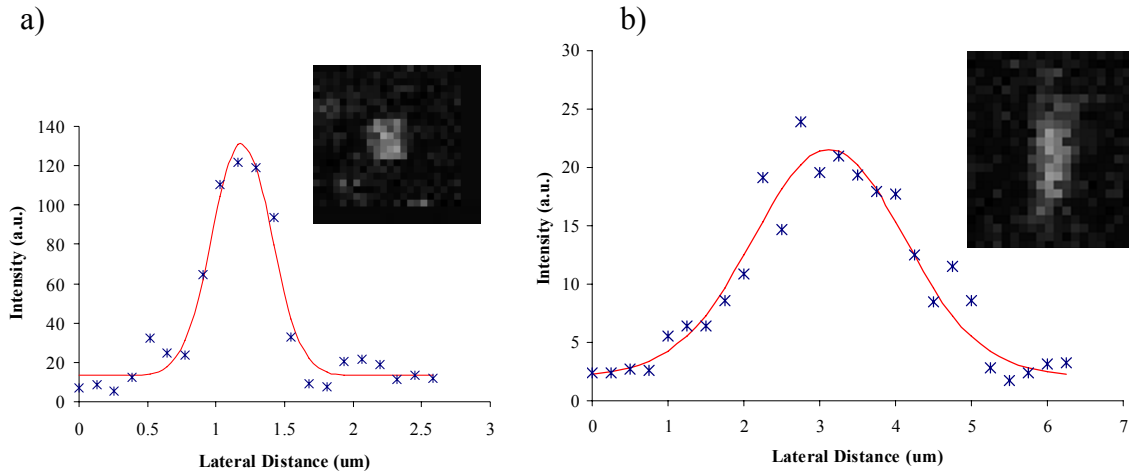

Figure 15: Gaussian Fit to the (a) radial and (b) axial PSF of a 100 nm fluorescent bead.

The expected theoretical resolution at the surface in TPM is calculated by using the equations for the 1/e-radius of the focal spot introduced by Zipfel and Webb [3]:

For NA>0.7: $w_{xy1/e} = \frac{0.325\lambda}{\sqrt{2}NA^{0.91}}$ $\qquad$ $w_{z1/e} = \frac{0.532\lambda}{\sqrt{2}}\left(\frac{1}{n-\sqrt{n^2-NA^2}}\right)$ $\qquad$ (2.5a)

The FWHM is obtained by multiplying the 1/e - radius (2.5a) with $2\cdot\sqrt{(\ln(2))}$. Using these equations, a numerical aperture of 0.95 (20x Olympus objective) and an excitation wavelength of 920 nm, the radial FWHM should be 370 nm and the axial FWHM

1440 nm. That the measured value is approximately twice the theoretical value might be explained by spherical aberrations introduced by infrared light while the objective is designed for visible light and the use of a 250 mm tube lens instead of a 180 mm tube lens. The reason for the mismatch of the tube lens is the necessary magnification of the laser beam as explained in section 2.4.4. High NA objectives are also often found to exhibit residual spherical aberration components of very high order.

2.5.3 Field of View

In microscopy, it is essential to know the real size and form of the imaging plane, the field-of-view (FOV), in order to measure objects accurately. In fluorescent scanning microscopy, the FOV depends on the scanning angle of the scanning mirrors. The dimensions of the FOV can be calibrated by imaging a fluorescent calibration grid or sample and changing its position in the x - and y - directions. We measured at the maximum deflection of the scanning mirrors an imaging area of 340 ± 10 µm in x- and y-direction, implying an accuracy of distance measurements of ± 3 %. Due to aberrations, the focal plane is also slightly bent, which results in a slightly curved FOV. This curvature contributes to the radial signal decrease that was observed and while imaging thin 2D planes (See Figure 14).

2.5.4 Spatial Uniformity

The homogeneity of the scan was determined by imaging a spatially uniform field of fluorescence. A petri dish filled with Rhodamine diluted in water was used for this experiment. This method detects inhomogeneities in the scan pathway, as well as in the detection pathway.

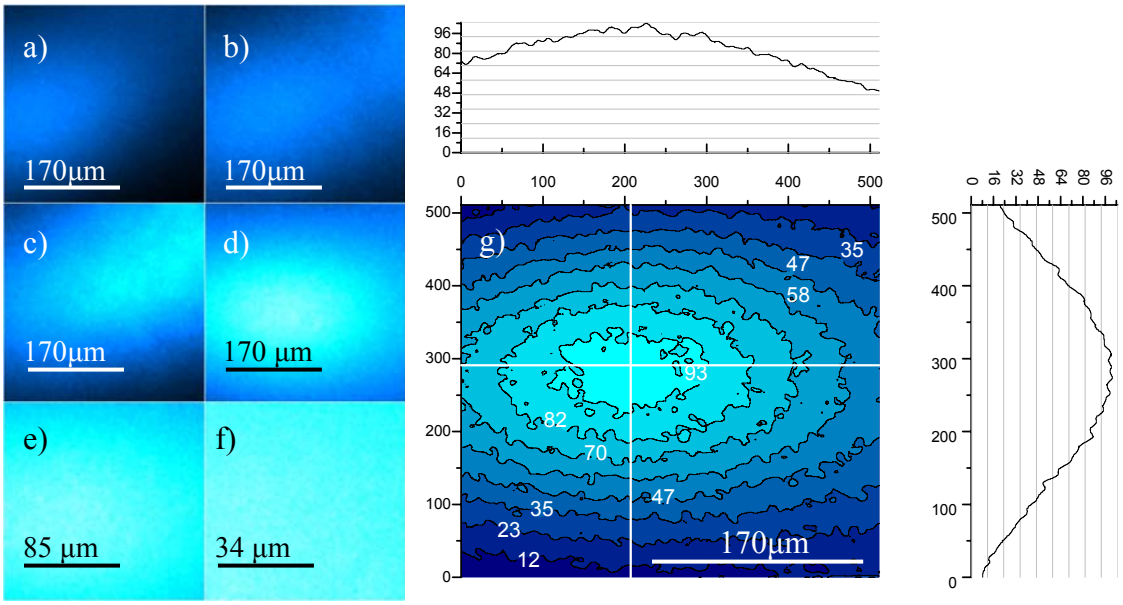

Figure 16: Imaging of a uniform fluorescence sample of a 340 x 340 µm field of view. The inhomogeneity of the scan (a) can be reduced by realigning the position of the PMT (b), (c) and by realigning the scan pathway (d). At a smaller field of view (e) 170 µm or (f) 68 µm, the intensity is almost uniform over the scanned area. The contour plot (g) shows the inhomogeneity of (d) quantitatively.

After realignment, the maximum FOV still shows inhomogeneity (Figure 16d) which is due to truncation of the scanning beam at the BA of the objective and at the small cathode of the PMT. The elliptical shape in Figure 16g might be reasoned by the intrinsic elliptical beam shape and residual misalignment. Nonetheless, this profile is stable for a given configuration of the TPM and thus can be used to calculate the real intensity over the scanned area of a taken image. Uniform images without further processing can be obtained by scanning a region smaller than the maximal FOV, of 100 x 100 µm. (See Figure 16e, f)

2.6 Imaging Results

This chapter shows images of flat and 3D samples, obtained with the presented two-photon microscope. The first samples are stained slides of epithelial cells and pollen which are commercial available (Figure 17 and Figure 18). Figure 19 shows fungus grown in a Petri dish. Figure 20 displays multiple order harmonic generation of a air bubble-gel interface. The scanned image data can be visualized in 3D as shown in Figure 21 and Figure 22. Unlike in Figure 17, which shows an overlay image of emission intensities at different excitation wavelengths, all other images are obtained at one particular wavelength and presented with a multi-color gradient instead of a gray scale.

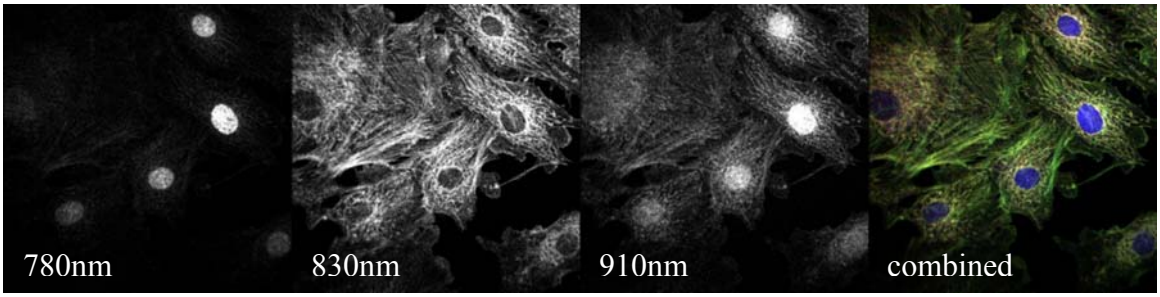

Figure 17: FluoCells® prepared slide #1. The excitation and emission of stains or fluorophores depends on the laser excitation wavelength, which is written under the image. The mitochondria are labeled with MitoTracker Red CMXRos and F-actin with BODIPY FL phallacidin (green). The nuclei are labeled with DAPI (yellow). The intensity maps at different excitation wavelengths can be overlayed with false colors (right). The thickness of this sample is only 8 µm which does not allow 3D scanning.

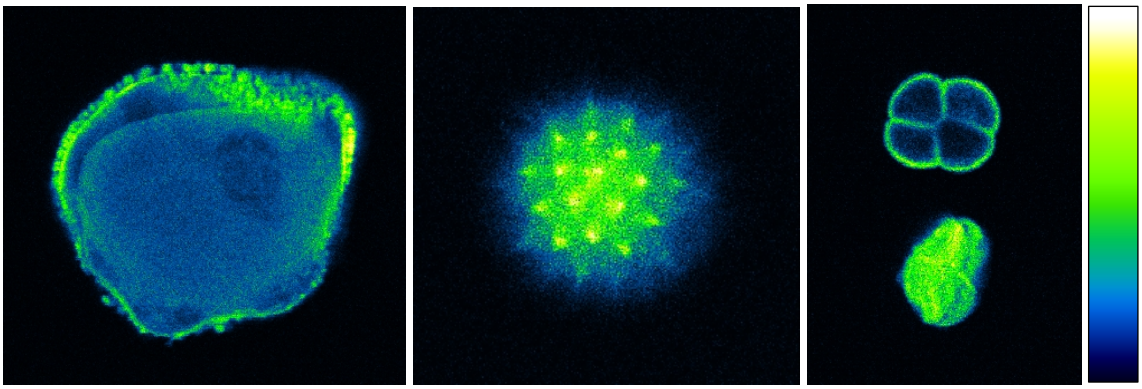

Figure 18: Pollen grains. The colors vary by intensity to distinguish better between different power levels. The bar on the right shows the gradient from no signal (black) to high signal (white).

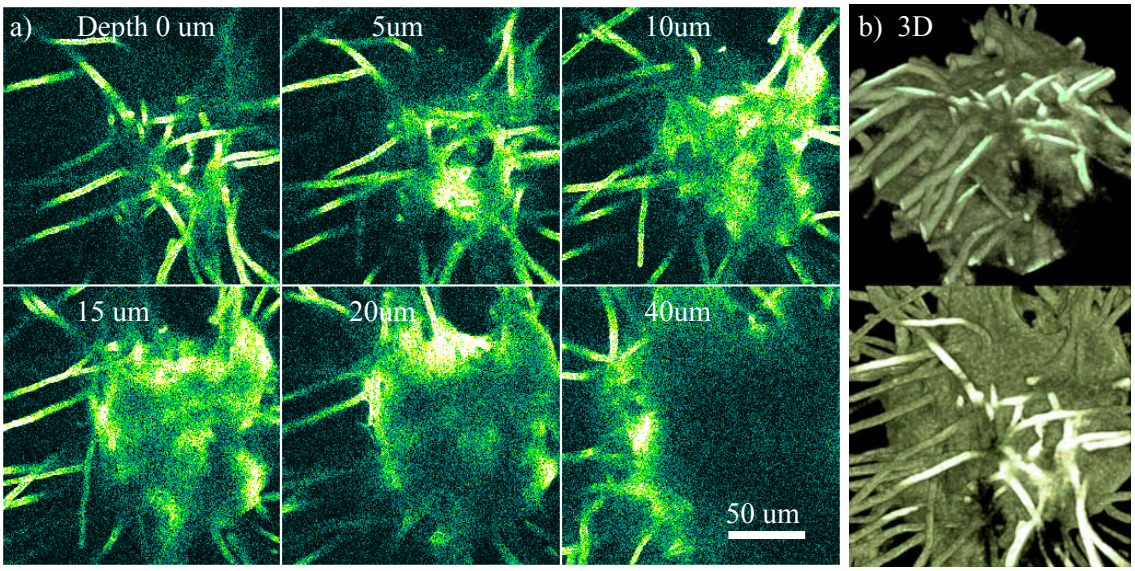

Figure 19: (a) Fungus imaged at different depth. (b) A detailed scan can be visualized in three dimensions.

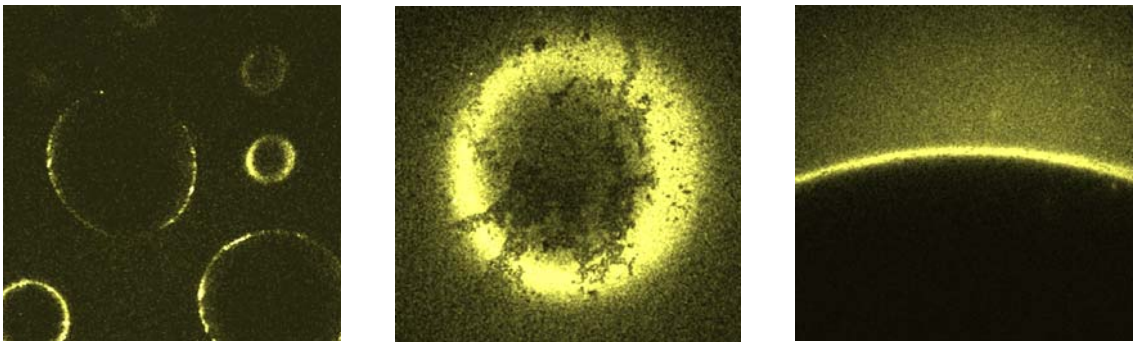

Figure 20: Harmonic Generation from air bubbles trapped in agar, recently explained in reference [24]. The signal is much stronger than from fluorescence. The image in the middle is the tip of a bubble sphere and the right picture shows the transition from agar to air.

To visualize the 3D structure of scanned specimen, we used a software tool called Voxx from the Indiana Center for Biological Microscopy. It allows to load a multi-page tiff-file (a stack) and to define transparency and red-green-blue values for each intensity value. 3D views help to understand the special structure of the sample and also to present the data to the public.

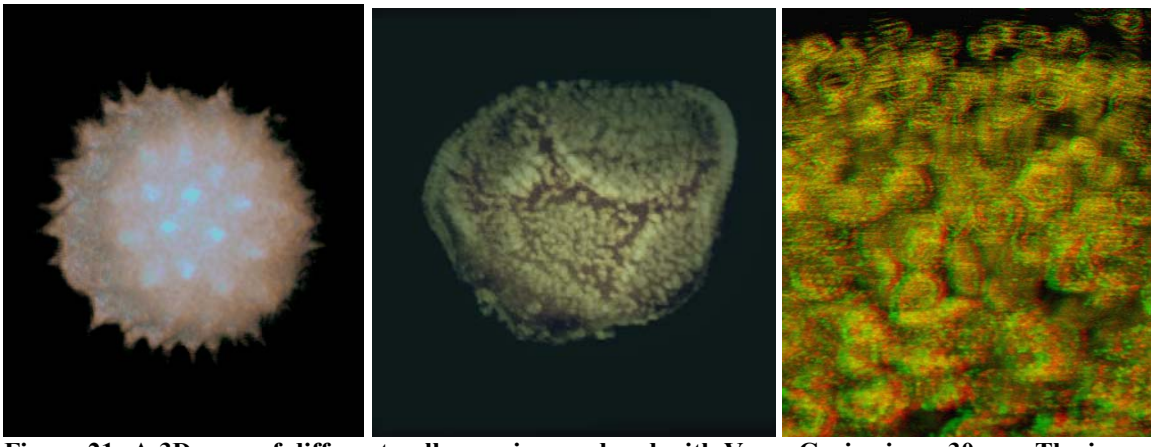

Figure 21: A 3D scan of different pollen grains rendered with Voxx. Grain size ≈ 30 µm. The image on the right shows cells in Anaglyph stereo mode which allows viewing the structure three dimensional using red-green glasses.

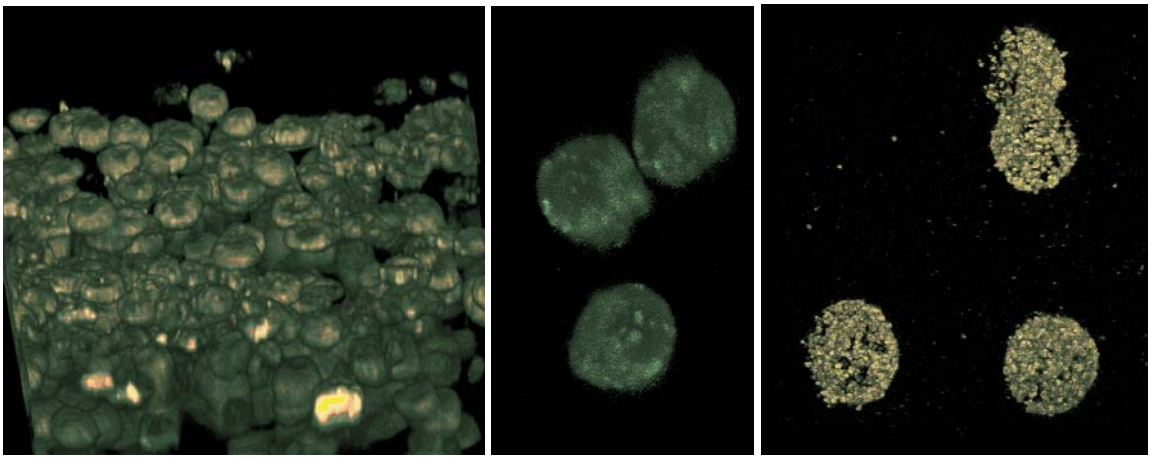

Figure 22: A stack of cells viewed from the side and single cells visualized in 3D with Voxx. The cells on the right are labeled with gold nanorods.

2.7 Improving the Acceptance Angle

An important part for deep imaging is the optimization of the collection of emission light. The collection optics need to be designed specifically to transmit as many rays as possible from the objective's back aperture (*BA*) onto the PMT cathode. Scattered emission rays may come out of the *BA* at angles up to 60 degrees. To collect as many rays from the *BA* as possible, a collection lens system must be chosen which images the complete *BA* onto the PMT cathode (See Equation 2.4c). The PMT used for the described TPM has a small cathode inserted inside a 9mm long cavity which blocks rays at steeper angles. Using a two-lens system or covering the walls of the collection pathway with reflective foil did not show any improvement in the collection efficiency. For further optimization of the collection, in this section the accepted angles depending on their exit position on the BA are investigated in detail for dichroic mirror, the collection lens, and the PMT. The main conclusion is that a PMT with a larger cathode is necessary to collect more emission light.

2.7.1 Acceptance Angle of the Dichroic Mirror

The dichroic mirror, which can be circular or rectangular, reflects from each point source from the *BA* a light cone or a light pyramid, respectively. In the following, maximum reflected angles are derived for rays which leave the *BA* in the middle up to rays which leave the *BA* on its margin.

As shown in section 2.3.3, the dichroic mirror will accept rays from its outermost margin up to 14°. Some rays from the *BA* will be reflected at larger angles as displayed in Figure 23b, depending on their original position on the *BA*. As the situation is not symmetric because of the 45° mirror mount, two axes need to be examined separately. The accepted angles depending on the position of the rays on the BA (Figure 23d) are calculated using the equations in Figure 23a. This graph shows, that some rays will be reflected from 14° up to 48° depending on the ray's origin and direction.

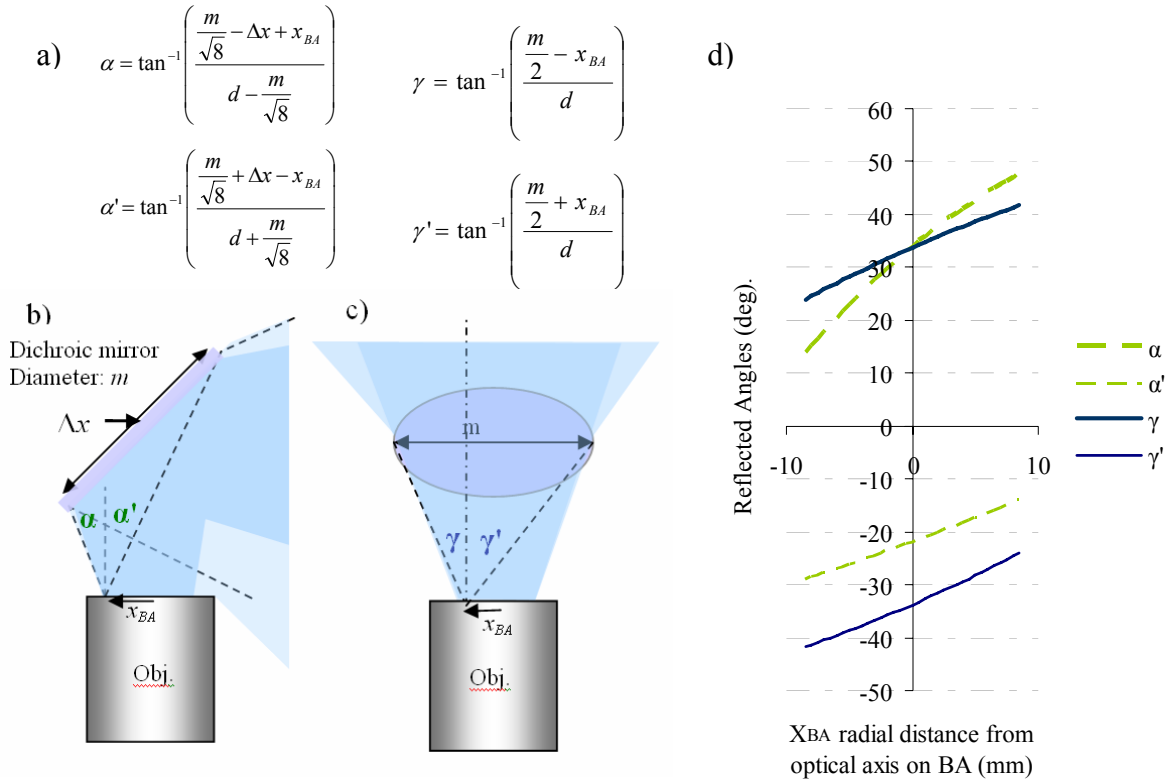

Figure 23: Maximum reflected angles leaving the *BA* at a distance x_{BA} from the optical axis. (b) The mirror reflection from the side. (c) The mirror reflection from behind. The equations (a) are plotted in (d).

2.7.2 Acceptance Angle of Lens and Photomultiplier Tube

The maximum acceptance angles for a ray leaving the objective at a distance x_{BA} are calculated using the equations in Figure 24. We next compare the acceptance angle of the dichroic mirror with the acceptance angle of lens and PMT

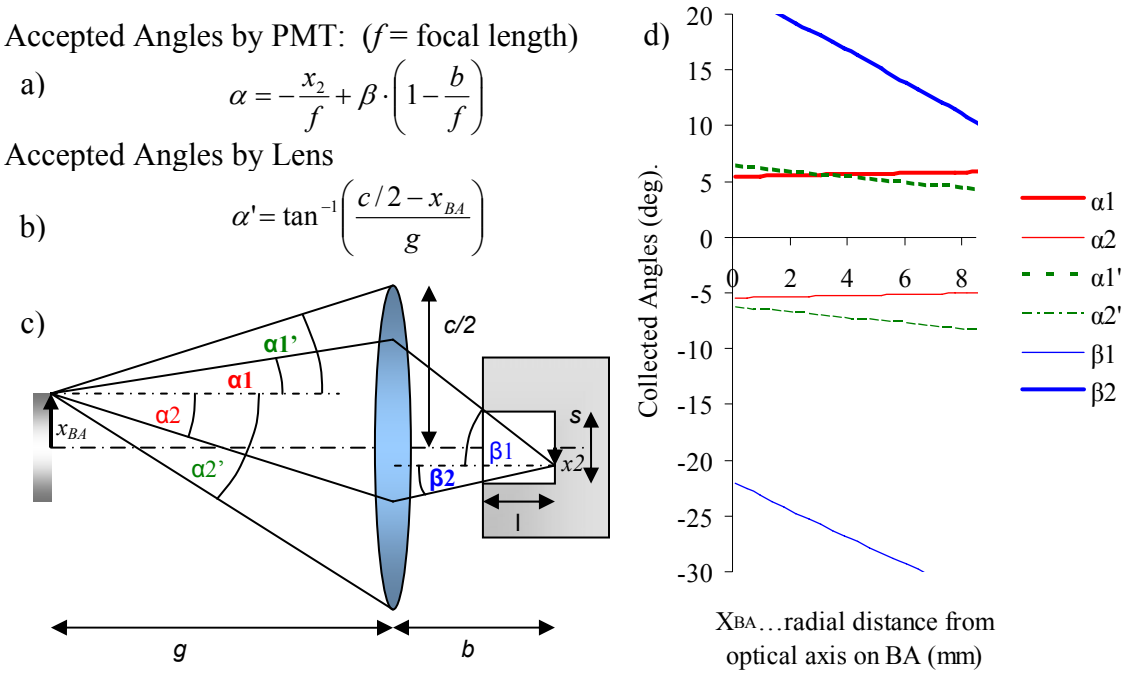

Figure 24: (c) The angular acceptance depends on the lens diameter *c* and the geometrical design of the PMT. (d) shows a plot of (a) and (b) with parameters from the current setup (See [6]).

Calculated with ray transfer matrix analysis, the accepted angles are -5.5° to 5.5° from the middle of the *BA* and -5° to 4.2° at its margin which is much less than the emission of the *BA*, and even less than the acceptance angle of the dichroic mirror.

To improve the angular acceptance, the lens needs to be closer to the *BA,* which can only be achieved using a PMT with a large exposed cathode. With short distances, the rays leave the lens at steeper angles and would hit the PMT housing in the current setup. Ideally the collection lens should be as close as possible behind the *BA,* which also increases the image size. The R3896 - PMT from Hamamatsu has an exposed cathode

with the dimensions 24 x 8 mm. A cathode with 24mm length would allow to move the lens much closer to the *BA*. Using a 2" lens (50.8 mm diameter) with f = 50.8 mm, a possible imaging condition is g = 83 mm and b = 125 mm. The angular acceptance of that system would be 11° - 20° and a 2" dichroic mirror would still be sufficient as seen in the comparison in Figure 25.

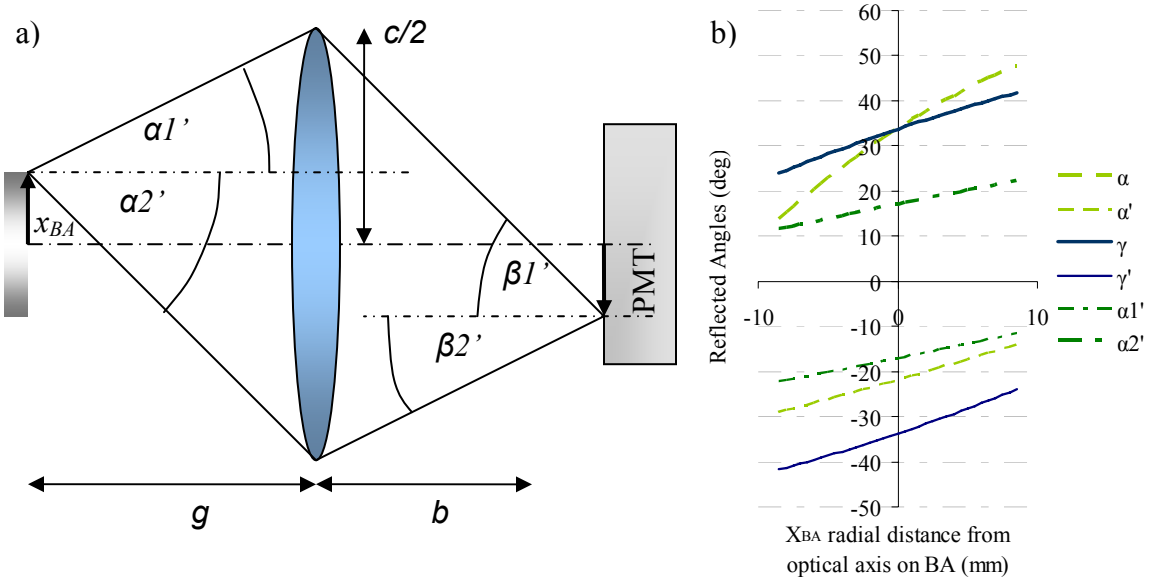

Figure 25: Calculation of the maximum acceptance angle independent of the cathode size in the PMT. (a) A collection system with a 2" collection lens (f = 50.8 mm) 83 mm away from the BA and a large exposed cathode. The acceptance angle is 11-20° depending on the initial position of the ray on the *BA*, compared to only 5° in the current system. (b) The accepted angles depending on x_{BA} show that a 2" dichroic mirror is still large enough for that system.

3 Study of the Imaging Depth Limit in Turbid Tissue

The imaging depth limit in tissue depends on such parameters as scattering, absorption and fluorescence distribution as well as on the specific design of the two-photon microscope. After a theoretical introduction to scattering and the description of optical properties of tissue, we show in this chapter our measurements of resolution and background fluorescence when imaging deep and present a 200 µm deep scan into a tissue phantom of cancerous cells. In the second part of this chapter we theoretically show how the optical parameters of tissue influence the generation and the collection of fluorescence independently. We finally conclude these investigations by presenting a wavelength range for optimal excitation and emission for deep imaging into tissue. This wavelength range can be reached with special contrast agents.

3.1 Theory of Light Scattering in Turbid Tissue

The propagation of light in a turbid sample depends strongly on its scattering properties. The scattering process occurs due to small particles in the sample and can be described with Mie theory. Two parameters describe scattering: first, the scattering coefficient μ_s and second, the scattering anisotropy g.

The scattering coefficient describes how much light will be scattered after traveling a distance z in a turbid sample.

$$P_{ballistic}(z) \propto P_0 e^{-\mu_S \cdot z} \qquad P_{scattered}(z) \propto P_0 (1 - e^{-\mu_S \cdot z}), \tag{3.1a}$$

while $P_{ballistic}$ is the part of the initial power P_0 which is not yet scattered in the depth z.
A more intuitive parameter to describe scattering is the average path of a photon until the next scattering event occurs: the scattering mean free path (MFP) $l_s = \mu_s^{-1}$. After light traveled the distance l_s in a scattering medium, 63 % of the initial light will be scattered.

The scattering anisotropy g describes the angular distribution of scattered light ranging from 1 to -1. A scattering anisotropy of g = 1 corresponds to pure forward directed scattering which equals to no scattering. g = -1 describes pure backward

scattering and for $g = 0$, light is scattered isotropically. The probability density function p for rays to scatter with the deflection angle γ can be calculated with Mie scattering approximation from Henyey and Greenstein [25]:

$$p(\gamma) = \frac{1 - g^2}{2(1 + g^2 - 2g \cdot \cos\gamma)^{3/2}} \tag{3.1b}$$

Figure 26 visualizes p for different scattering anisotropies.

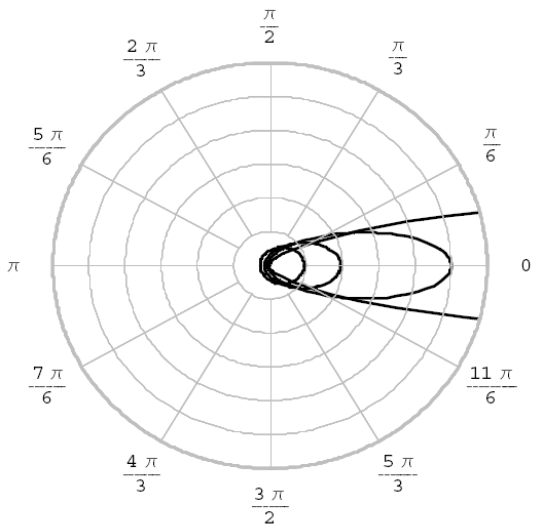

Figure 26: Polar diagram of Equation 3.1b, the Henyey-Greenstein probability density function for different anisotropy factors g = 0.2, 0.4, 0.6 and 0.8 (Source: [26]).

The light path through a sample depends strongly on the scattering anisotropy. A common factor to describe it through a turbid media is the transport MFP, $l_t = l_s/(1-g)$, which is the reciprocal of the reduced scattering coefficient, $\mu_s' = \mu_s(1-g)$. Nevertheless, it does not help to describe the amount of photons reaching the focal spot in a turbid medium because even slightly scattered photons miss the focal spot which is less than 1 µm wide. Thus, we will not use the transport MFP in this sample and optical properties will be given with the common scattering MFP.

3.2 Optical Properties of Epithelial Tissue

Imaging with light deep into samples depends mostly on four optical parameters: The refractive index n, the scattering coefficient μ_s, the scattering anisotropy g and the absorption coefficient μ_a. It is essential to study the role of each of these parameters in order to simulate photon propagation and to design and optimize instruments for deep tissue imaging.

In most biological tissues, the refractive index ranges from 1.33 (water) to 1.6 (melanin in the epidermal layer of the skin). However, the effective index of refraction for most tissues is approximately 1.4. Hence, using water as an immersion fluid will lead to less aberration than using oil as an immersion fluid with an index of refraction of 1.51. A list of refractive indices for tissues and tissue constituents can be found in [22]. Figure 27 presents scattering and absorption parameters of brain, skin, and cancerous skin, that were recently measured by Yaroslavsky et al. using integrating sphere spectrophotometer techniques [27], [28].

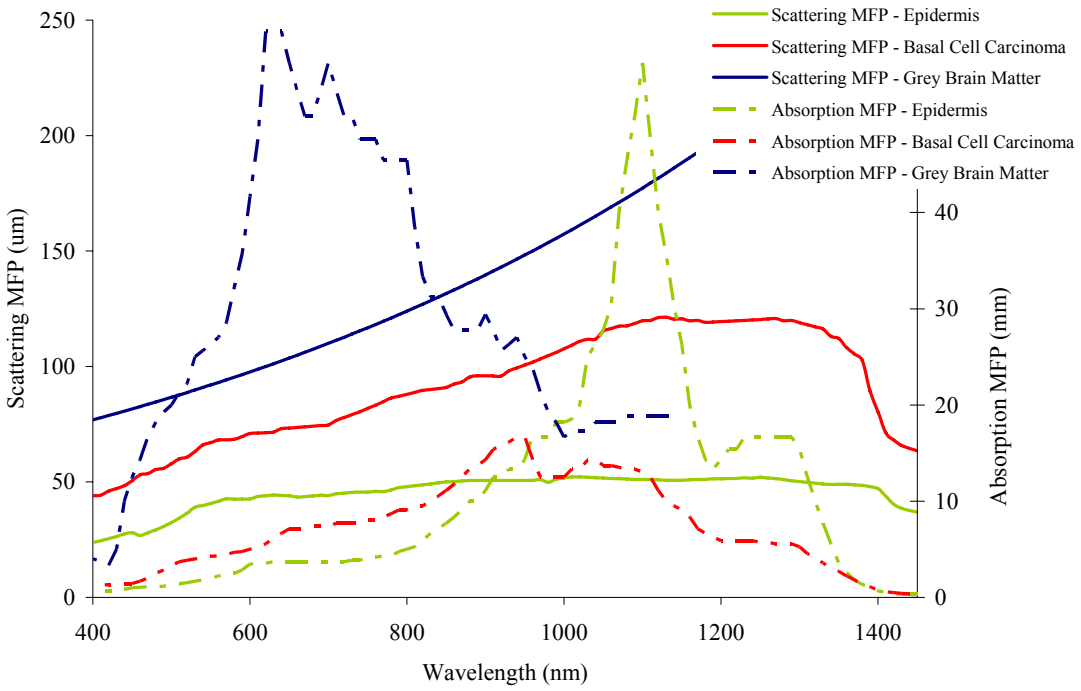

Figure 27: Scattering MFP and Absorption MFP from skin epidermis, basal cell carcinoma (BCC) [27], and grey brain matter [28].

Imaging into brain has been performed up to more than a millimeter deep [29]. The reason is clearly visible in Figure 27. The scattering MFP in brain matter is three times longer compared to epidermis, which allows threefold deeper penetration (See Equation 2.3a. Moreover, brain tissue absorbs less light, especially in the emission range, which means the collection efficiency is also much higher than in the epidermis.

To measure the performance of the new TPM versus depth in turbid media, we prepared samples with 2% Intralipid and fluorescent beads. The particles in Intralipid scatter light and depending on the concentration of Intralipid, the scattering and absorption properties can be varied. Based on the measurements from van Staveren et. al. [30] and Flock et. al. [31], the optical properties of this sample are as displayed in Figure 28. According to Dunn [32], these optical properties are comparable to cervical tissue [33].

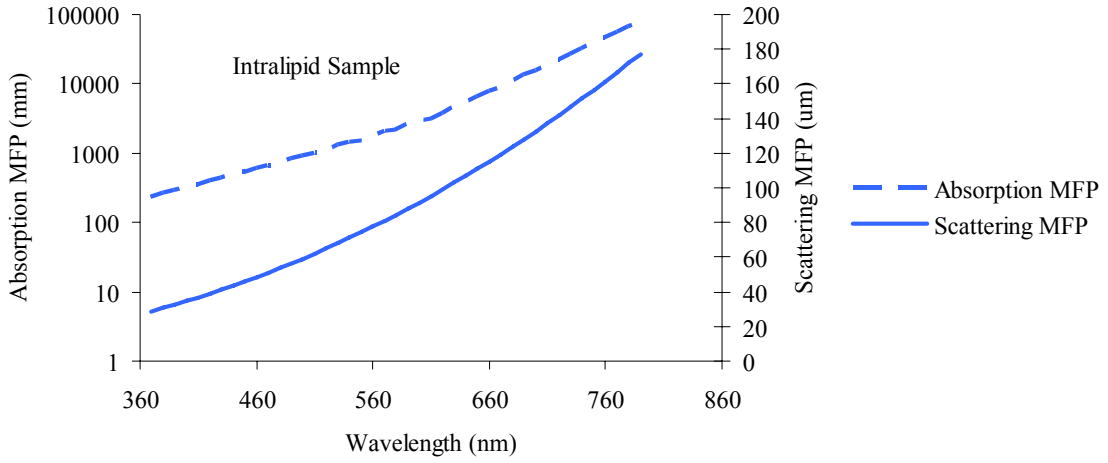

Figure 28: Absorption and scattering properties of 2% Intralipid as taken from [30] and [31]. Intralipid was used to simulate scattering conditions of real tissue.

Another important property of the sample for TPM is its excitation and emission spectra of its fluorophores. Living tissue has molecules which are autofluorescent. One dominant molecule in living tissue is NADH. The excitation maximum of NADH ranges

from 700 nm to 750 nm and its emission from 400 nm to 600 nm (See Figure 29) [34]. As Figure 27 shows, for deep imaging into the epidermis it would make sense to move to higher wavelengths in the excitation and also in the emission. This can only be achieved by using special dyes or contrast agents which have different excitation and emission spectra. Promising contrast agents are gold nanorods because they are non-toxic, produce more emission signal at higher wavelengths (See Figure 29) and can especially target cancerous cells [6].

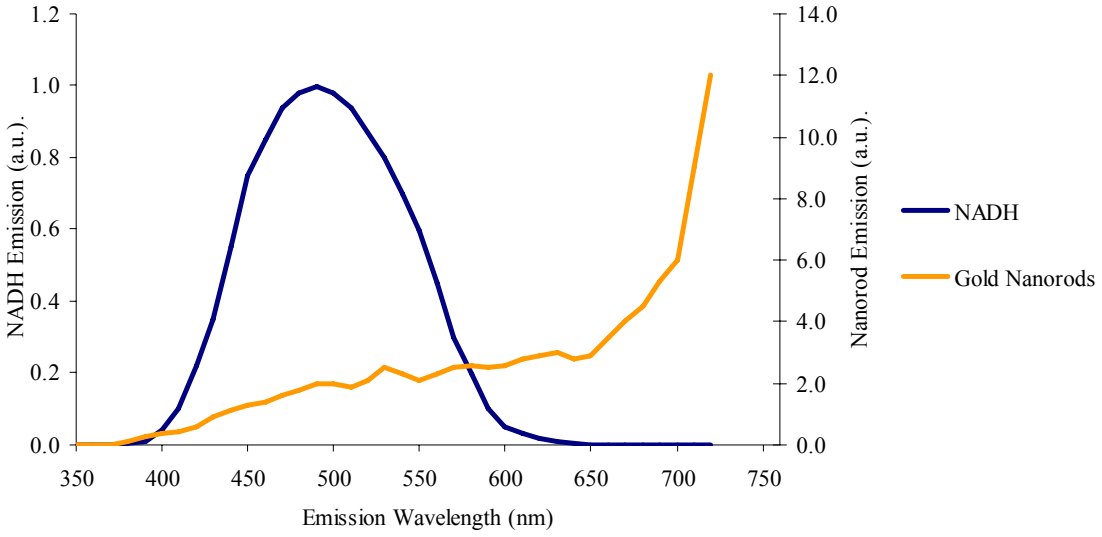

Figure 29: Emission spectra of fluorescent NADH [34], [35] and 760 nm resonant Nanorods (16 x 48 nm rods) [36], [37].

3.3 Measurements on Deep Imaging in Turbid Media

The main purpose of the assembled TPM is to study deep imaging in turbid media. With the setup as described in Chapter 2, resolution and signal to background ratio (later denoted with *Sgn/Bkg*) was measured for different imaging depths. Moreover, deep imaging into a dense cancerous tissue phantom was performed with unlabeled autofluorescent cells as well as with nanorod labeled cells.

3.3.1 Resolution depending on the Imaging Depth

We used 100 nm fluorescent beads (FluoSpheres® F8803, Molecular probes), mixed homogeneously in a solution of 2% intralipid and 98% agarose to simulate optical properties of cervical tissue [33], [32]. Imaging was possible down to 250 μm until the background signal was too large to identify single beads. The imaging depth can be improved by preparing samples with lower bead concentration. The PSF measurements showed large deviations due to difficulties in separating signal and noise. Nevertheless a linear fit reveals a slight increase in radial resolution with depth and a slightly larger increase of axial resolution.

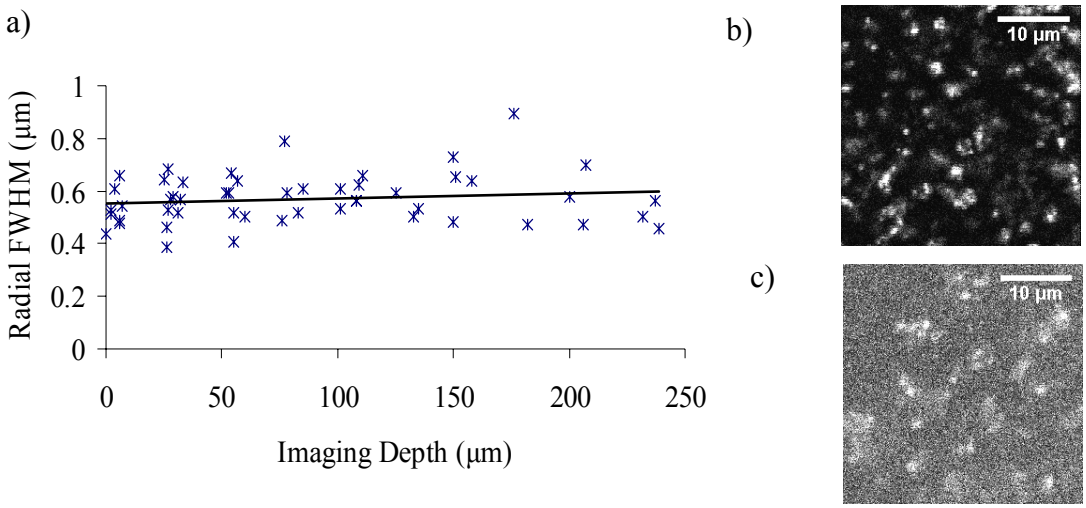

Figure 30: (a) Radial Resolution dependence on the imaging depth in a turbid medium with a scattering MFP of estimated 150 µm. The PSF was acquired from 100 nm fluorescent beads in an agar - intralipid mix. The black function delineates a linear fit to the acquired data. Figure b) shows an image of beads close to the surface. Figure c) illustrates the increase of background signal at 250 µm deep.

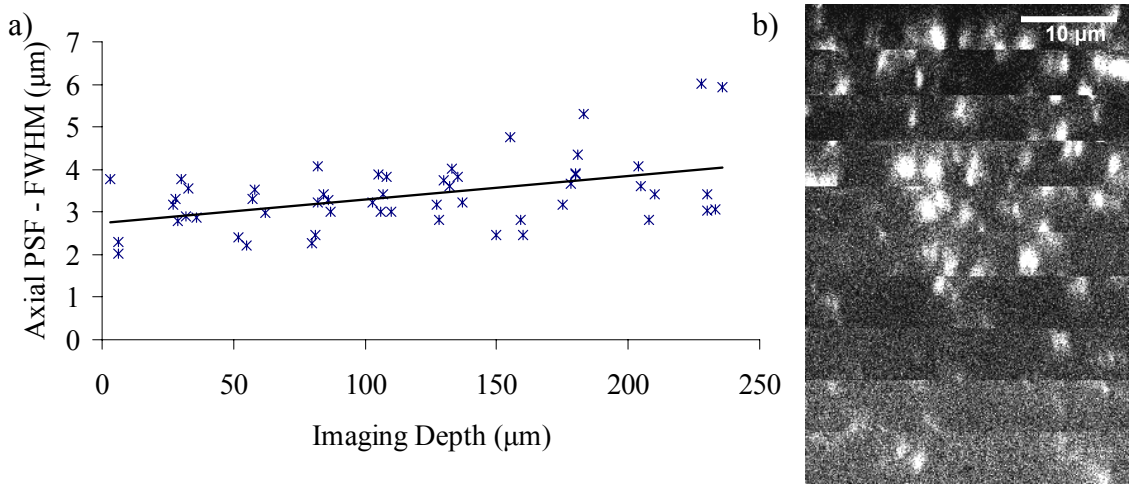

Figure 31: (a) Axial Resolution dependence on the imaging depth in turbid media with an estimated scattering MFP of 150µm. The PSF were measured from a detailed *z*-scan: Every 25µm in depth, a stack of 40 images with 0.25µm displacement was acquired. (b) shows the *x*-*z* - reconstruction processed with the program ImageJ.

3.3.2 Signal to Background Ratio

The bead-agar-2%intralipid mix was also used to measure the increase of background noise with imaging depth by averaging the signal from an image area without beads. Figure 32 shows the exponential increase of power and the exponential decrease of *Sgn/Bkg*. A measurement with different excitation wavelengths showed that the *Sgn/Bkg* decreases slower with longer wavelengths, which is the result of less scattering and absorption at higher wavelengths (data not shown).

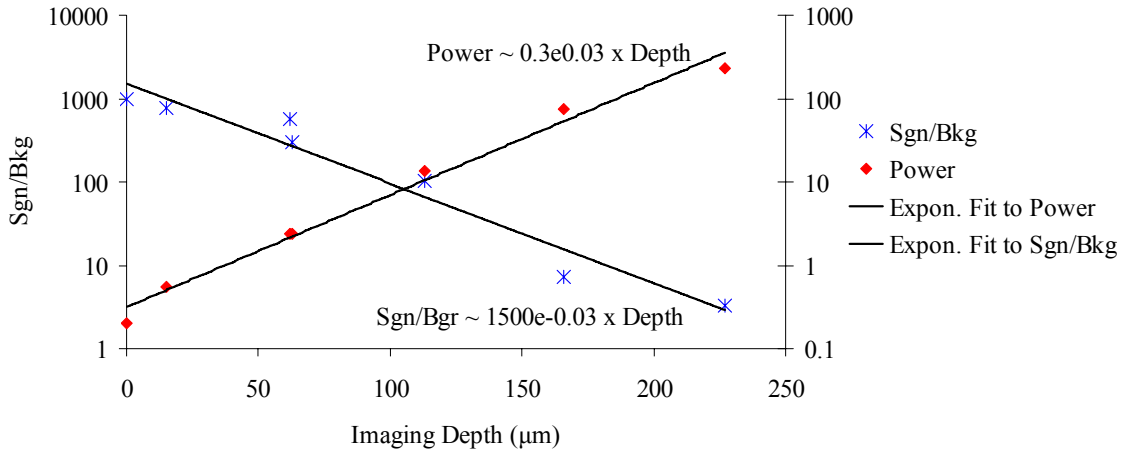

Figure 32: Signal to background ratio (*Sgn/Bkg*) for different imaging depths. To obtain the same signal in depth, the laser power has to be increased exponentially. This causes also an exponential increase of surface fluorescence which explains the exponential decay in *Sgn/Bkg* with depth.

3.3.3 Imaging Cancerous Tissue Phantoms in Three Dimensions

Three-dimensional conglomerations of cancerous cells (tissue phantoms) were prepared as described in [6]. The maximum imaging depth was approximately 200µm which is twice the imaging depth than reached with a previously home-built inverted TPM in our lab. The increased imaging depth is mainly due to the new water immersion objective as compared to oil immersion objective used in the inverted TPM setup. Moreover, imaging with nanorods improved the image quality and decreased the necessary laser power (See Figure 34 and Figure 35).

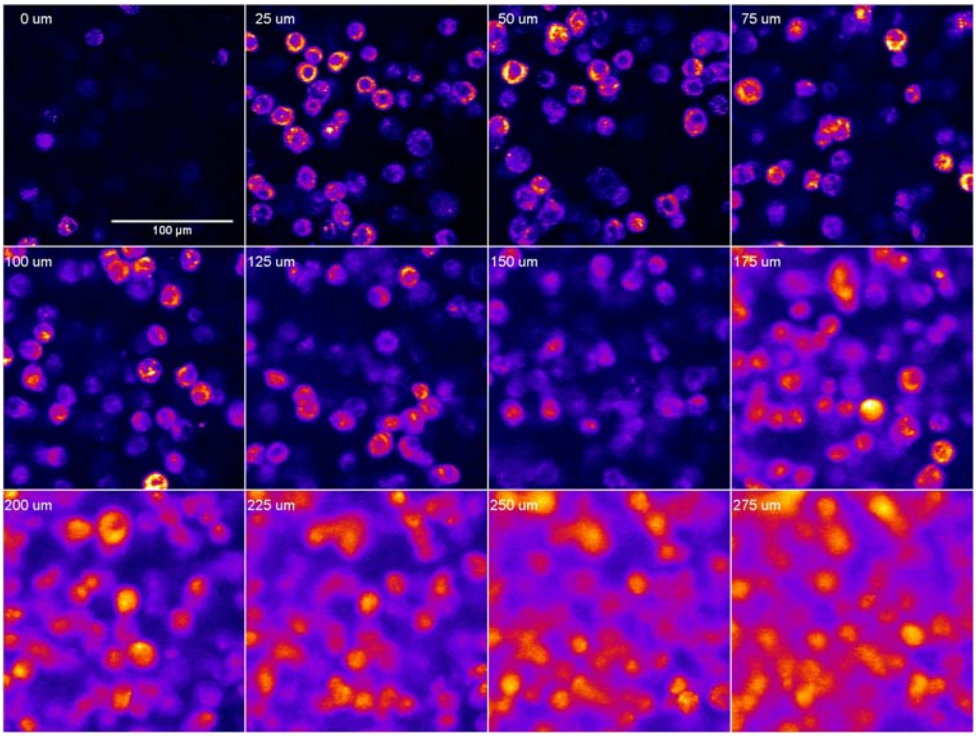

Figure 33: Two-photon autofluorescence images of a cancerous tissue phantom at different depths.

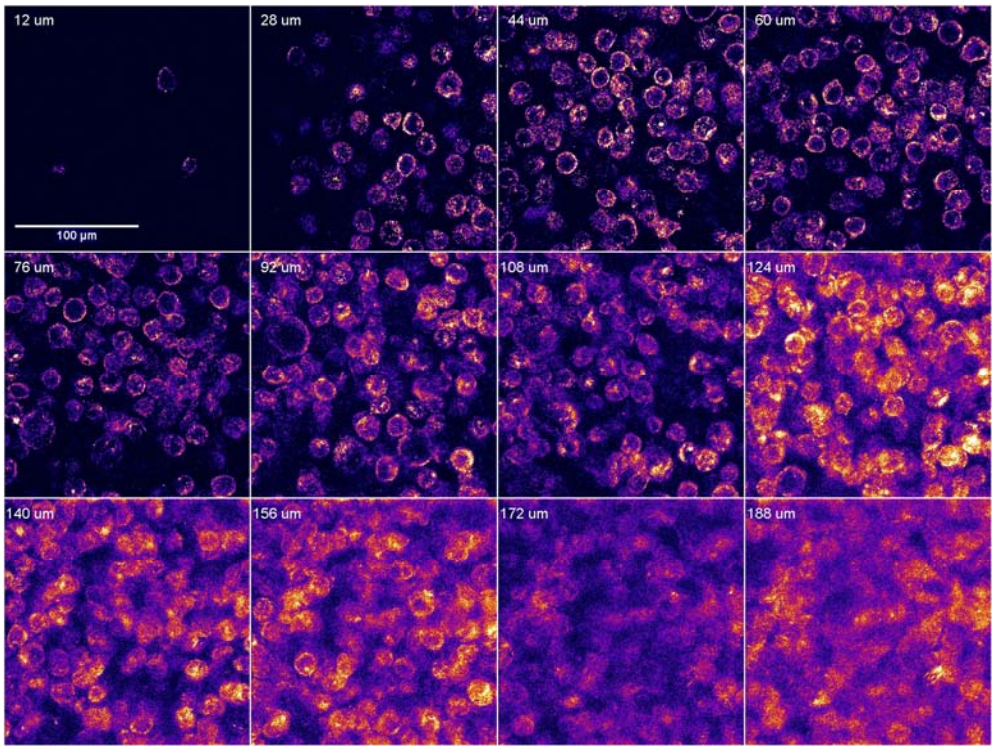

Figure 34: Two-photon photoluminescence images of a nanorod labeled cancerous tissue phantom at different depths.

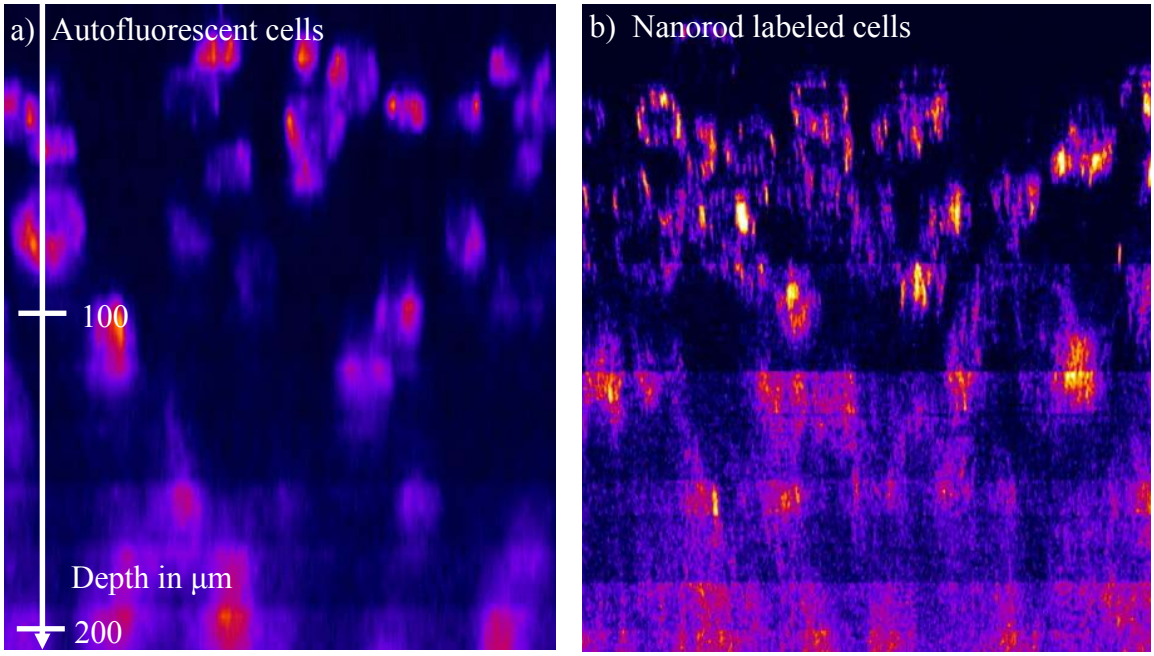

Figure 35: x-z reconstruction from (a) autofluorescent unlabeled cells (autofluorescence) and (b) nanorod labeled cells(luminescence). The vertical slice was processed out of the 3D image stack (Figure 33 and Figure 34), using the program ImageJ. The numbers on the right side of each image display the laser power at the particular depth. The comparison shows that nanorod labeled cells improve the image contrast and require less excitation power for the same generation of fluorescence.

3.4 Calculation of Fluorescence Generation

In the present and the following sections, we study the fluorescence generation and collection separately in order to understand how optical parameters of the sample influence the imaging depth limit. This knowledge is important in order to find ways to extend this limit. We calculate the generation of fluorescence in the whole sample with analytical approximations that describe the propagation of focused light in turbid media [26]. Scattered as well as unscattered (ballistic) photons contribute to out-of-focus fluorescence. After deriving the intensity distribution of scattered and ballistic photons, the generated focus and out-of-focus fluorescence is calculated and displayed for a few examples. The fundamental imaging depth limit as defined by Theer and Denk [5] is the depth where the generation of total out-of-focus fluorescence is equal to the fluorescence generated at the focal point (See Equation 2.3b). This section clarifies that in tissue, scattering primarily leads to background fluorescence and that scattering of excitation light is thus the critical factor which limits the imaging depth. Figure 36 shows the parameters that influence the focus and out-of-focus fluorescence generation.

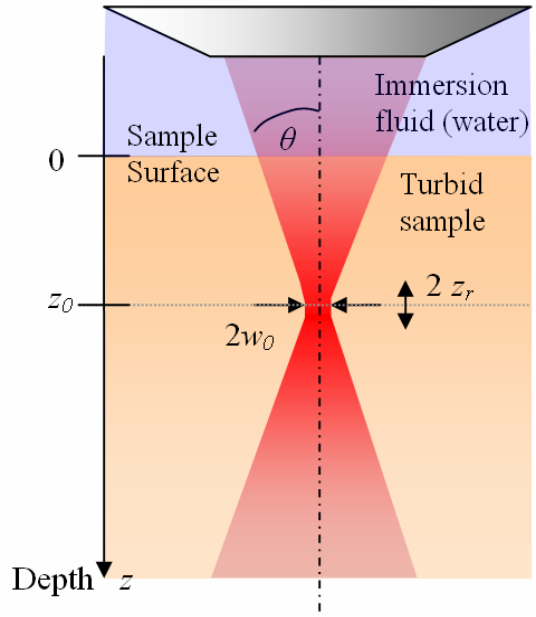

l_s: Scattering MFP
l_a: Absorption MFP
g: Scattering Anisotropy
n: Refractive Index
z_0: Imaging Depth
z_r: Rayleigh Range

The following variables define the $1/e^2$ width:

w_0: Beam Waist Radius
τ_0: Pulse Duration
θ: Divergence Angle

$$\theta_{1/e^2} = \theta = \sin^{-1}\left(\frac{NA}{n}\right) \qquad (3.4a)$$

Figure 36: Schematic of the focused Laser beam to explain the parameters used to calculate the fluorescence generation.

3.4.1 Distribution of ballistic laser light

The ballistic laser photons reach the focal spot and generate signal fluorescence. They will also contribute to background fluorescence from the surface as for deep imaging high laser powers are necessary in order to deliver enough photons to the focal spot. In this sub-section, the beam waist of a laser focused into a turbid sample will be derived depending on depth z and imaging depth z_0.

The intensity distribution of a Gaussian laser beam focused in a medium without scattering or absorption depending on the axial distance z (depth), the radial distance $\rho = \sqrt{x^2 + y^2}$ and the time t is given by:

$$I(z,\rho,t) = \frac{2P(z,t)}{\pi w^2(z)} e^{-\frac{2\rho^2}{w^2(z)}}, \tag{3.4b}$$

with the beam waist radius $w(z)$ and the power P in depth z. The beam waist radius w_{00} at the focal point and its Rayleigh range z_{r0} are commonly defined by [38]:

$$z_{r0} = \frac{\lambda}{n \cdot \pi \cdot \theta^2} \tag{3.4c}$$

$$w_{00} = \frac{\lambda}{n \cdot \pi \cdot \theta}, \text{ while } w_{00}^2 = \frac{\lambda \cdot z_{r0}}{n \cdot \pi} \tag{3.4d}$$

In a fluorescent medium with scattering and absorption, out-of-focus light will be generated in addition to light generated at the focal spot. The out-of-focus light will reduce the signal to noise ratio and might eventually be the limiting factor for deep imaging. The attenuation coefficient α, as well as the average staining inhomogeneity χ have the strongest influence on the out-of-focus light generation:

$$\alpha = \frac{1}{l_s} + \frac{1}{l_a} \tag{3.4e}$$

$$\chi = \left\langle \frac{Total\_Volume}{Fluorescent\_Volume} \right\rangle \tag{3.4f}$$

If the staining of a sample is defined by the ratio of stained volume to total volume, the average staining inhomogeneity will be the reciprocal of the staining. The staining

inhomogeneity is different for every sample and difficult to estimate. Therefore it is hardly possible to calculate an accurate depth-limit for every real sample.

Scattering influences the beam width at the focal point. It can be derived from the spherical wave solution to the telegrapher's equation and the Fresnel approximation [26]:

$$w_{ballistic}(z) = \sqrt{\frac{4\lambda\left((z-z_0)^2 + z_r^2\right)}{4\pi \cdot n \cdot z_r + \lambda\alpha \cdot (z-z_0)}} \tag{3.4g}$$

A good approximation for z_r and w_0 at the focal point is then given by:

$$z_r \cong z_{r0} + \frac{\alpha \cdot \lambda}{4\pi \cdot n} z_0 \qquad\qquad w_0 \cong \sqrt{w_{00}^2 + \frac{\alpha \cdot \lambda^2 \cdot z_0}{4\pi^2 \cdot n^2}} \tag{3.4h}$$

These equations describe the slight increase of radial and axial PSF with imaging depth as observed experimentally in section 3.3.1.

3.4.2 Distribution of scattered laser light

All of the scattered laser light will contribute to out-of-focus fluorescence. The distribution of scattered laser light is difficult to estimate. The variance of its spatial and temporal distributions can be calculated using the approach introduced by McLean et al. [39]. Including these variances into the initial beam width and pulse length, the effective beam width $w_{scat\text{-}eff}$ and pulse width $\tau_{scat\text{-}eff}$ for the scattered light depending on the depth are:

$$w_{scat-eff}(z) = \sqrt{w_0^2 \cdot \left(1 + \frac{(z-z_0)^2}{z_r}\right) + \frac{4}{3}\frac{z^3}{l_s}(1-g)} \tag{3.4i}$$

$$\tau_{scat-eff}(z) = \sqrt{\tau_0^2 + \frac{8}{9}\frac{z^3}{c^2 \cdot l_s}(g-2)(g-1) + \frac{4}{6}\frac{z^4}{c^2 \cdot l_s^2}(1-g)^2} \tag{3.4j}$$

Figure 37 visualizes the variation of these two parameters for scattered light in a typical imaging configuration.

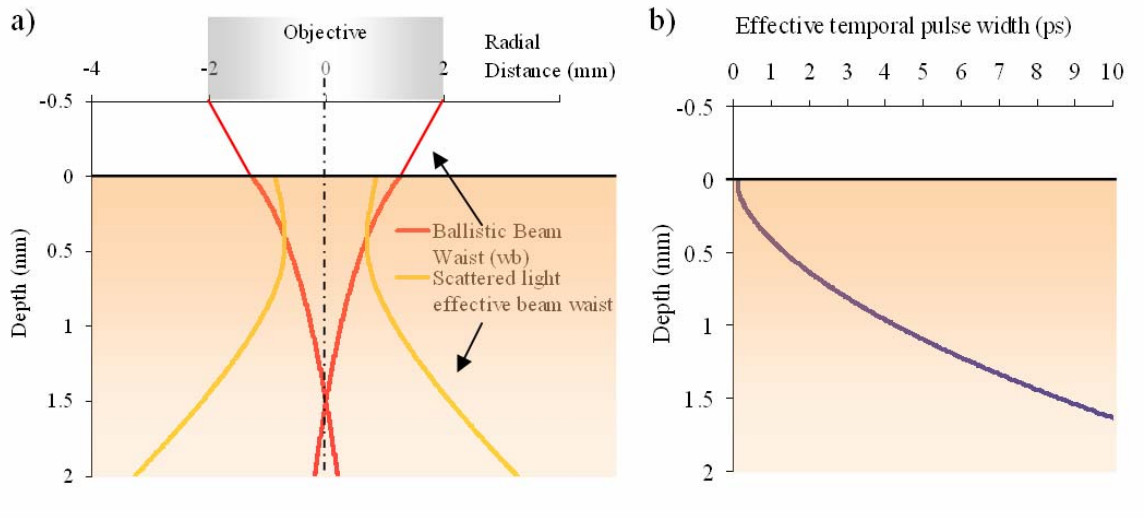

Figure 37: (a) Visualization of the beam waist of ballistic light (3.4g), and of the effective beam waist of scattered light in turbid media (3.4i). (b) Spread of the effective temporal pulse width of scattered light in turbid media of an initial 100fs pulse based on (3.4j). Parameters for these calculations: $NA = 0.95$, $\lambda = 900$ nm, $g = 0.9$, $l_s = 100$ µm, and $z_0 = 1.5$ mm.

3.4.3 Calculation of Fluorescence Generation in Turbid Tissue

In TPM, the generated fluorescence scales with the square of the laser intensity. The intensities are given by Gaussian distributions and depend on time and space (See Equation 3.4b). An accurate calculation of the fluorescence distribution could be determined by the integration of excitation light intensity over time and space. However, in this thesis, general tendencies are investigated and thus only proportionality was considered and intensities were calculated using top-hat beam approximations:

$$I_{ball}(z) \propto \frac{P_{ball}(z)}{w_{ball}^2(z)} \quad \text{with} \quad P_{ball}(z) \propto \frac{E_0}{\tau_0} e^{-\alpha \cdot z} \tag{3.4k}$$

$$I_{scat}(z) \propto \frac{P_{scat}(z)}{w_{eff-scat}^2(z)} \quad \text{with} \quad P_{scat} \propto \frac{E_0}{\tau_{scat-eff}(z)} (1 - e^{-\frac{z}{l_s}}), \tag{3.4l}$$

where E_0 is the pulse energy at the surface of the sample. The powers are derived using (3.1a).

The overall fluorescence generated from a plane at a depth z is then proportional to the square of ballistic and scattered laser intensities multiplied by the excited volume at this depth.

$$F(z) \propto \left(I_{ball} + I_{scat}\right)^2 \cdot dV \cong \left(I_{ball}^2 \cdot w_{ball}^2 + I_{scat}^2 w_{scat-eff}^2 + 2 \cdot I_{ball} \cdot I_{scat} \cdot w_{ball}^2\right) \cdot dz \qquad (3.4m)$$

Figure 38 presents an example solution for the contribution of ballistic and scattered light to out-of-focus fluorescence.

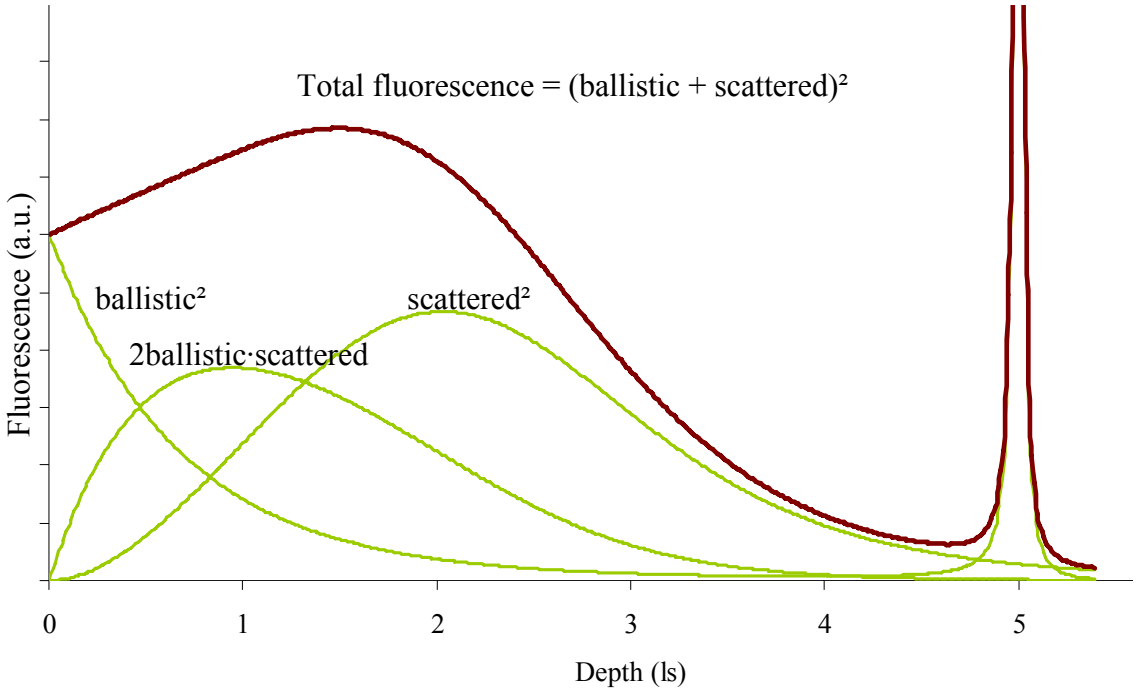

Figure 38: Example of the contribution of ballistic and scattered light to out-of-focus fluorescence. For every depth, the graph shows the integrated fluorescence over the whole plane at this particular depth.

3.4.4 Results

Figure 38 clearly shows that almost none of the scattered light will contribute to fluorescence from the focal spot. The scattered light reaching the depth z_0 is spread over a large area (See Figure 37a) and is unlikely to reach the small focal spot. All the scattered light proceeds to create more background fluorescence. The laser power attenuation deep within the tissue is mostly due to scattering as l_a is 50 to 500 times larger than l_s (See Figure 27). It was also found that the background fluorescence generation is stronger for

shorter l_s at the same imaging depth in terms of l_s. Hence, it is appropriate to consider l_s as the main factor of the sample which influences the generation of signal and background fluorescence depending on depth, and thus the imaging depth limit.

Out-of-focus fluorescence is generated over the whole volume from the surface down to the focal point. It is interesting to note that out-of-focus fluorescence reaches a maximum not at the surface, but at a depth between the surface and the focal spot. The depth of this maximum mostly depends on the scattering anisotropy g as demonstrated in [5] because g influences the minimal waist of $w_{scat\text{-}eff}$. The depth of this maximum background fluorescence also stays similar for different imaging depths as our calculations show (Figure 39).

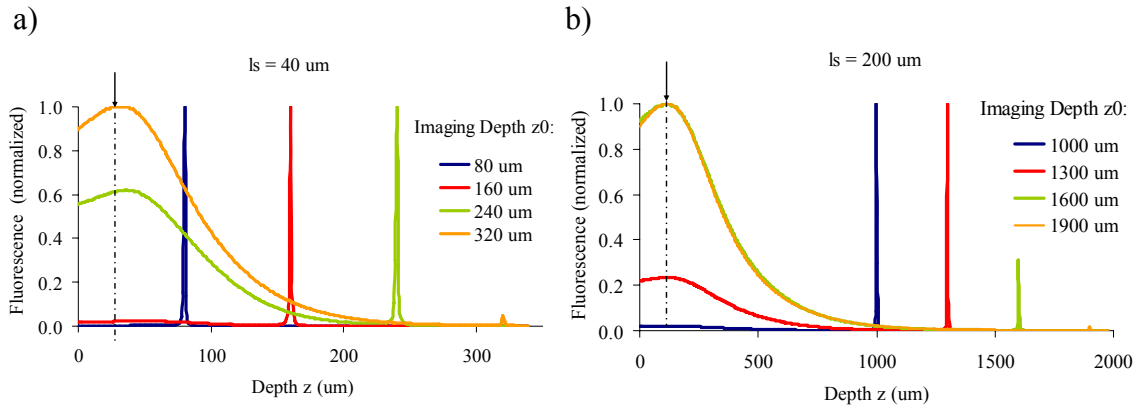

Figure 39: Plot of focal and out-of-focus fluorescence at different imaging depths for (a) l_s = 40 µm and (b) l_s = 200 µm. Note that the depth of maximum fluorescence (arrow) stays almost constant for different imaging depths.

To study the collection of the generated fluorescence, it is important to know the spatial distribution of the out-of-focus fluorescence. The intensity distribution of fluorescence due to scattering and absorption can be calculated using Equations 3.4b, 3.4g, 3.4i, 3.4k, and 3.4l. Figure 40 displays this calculation for an epidermis-like sample at an imaging depth far beyond the imaging depth limit in order to clearly demonstrate the distribution of out-of-focus fluorescence in general.

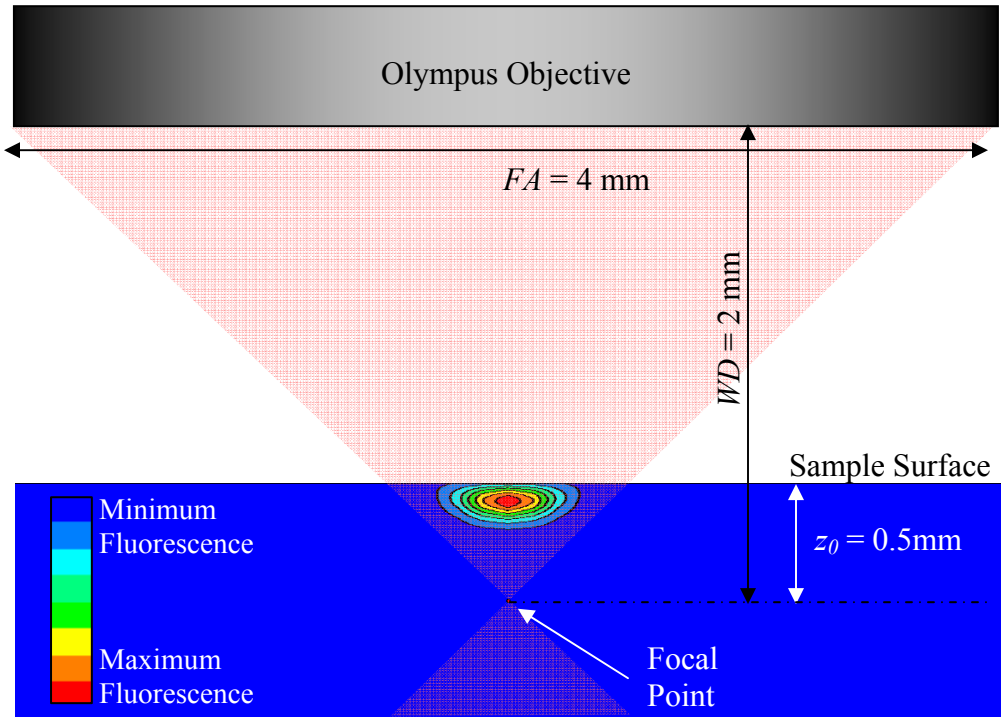

Figure 40: The distribution of out-of focus fluorescence generation during deep imaging into a tissue-like turbid media. Fixed epidermis-like parameters: l_s = 44 µm, l_a = 3700 µm, g = 0.82.

In conclusion, we have shown in this section that the fluorescence generation from the focal spot is mostly limited by the scattering of laser light and that out-of-focus fluorescence is generated in a large ellipsoidal volume close to the surface. This out-of-focus fluorescence will be collected by the objective lens as background and will exceed the signal generated at the focal point. For deep imaging in tissue it is important to use excitation wavelengths with a large scattering MFP in the tissue. In epidermis, the wavelength range with least scattering is approximately 1000 to 1400 µm (See Figure 27). The excitation maximum of autofluorophores in tissue as NADH ranges from 700 to 750 nm [34]. To image deeper, it is therefore necessary to apply contrast agents into the tissue with an excitation maximum at a wavelength with minimal scattering.

3.5 Calculation of Fluorescence Collection

In the previous section we showed that fluorescence is generated at the focal spot of the laser and over a large area close to the surface. The next step is to calculate how much of this fluorescence can be collected by the objective and which parameters influence the collection efficiency. It has already been shown [40] that large NA, large field of view and scattering increase the collection efficiency in specific cases. To our knowledge no one investigated how the origin of the emission light and how different absorption and/or scattering parameters influence the collection efficiency. We do so in this section. We show that the collection efficiency is different for emission from the focal spot and emission from out-of focus and see also that absorption is the main parameter which limits the fluorescence collection from deep within tissue.

At the beginning of this section, theoretical marginal cases are investigated to understand the influence of scattering and absorption on fluorescence collection independently. Subsequently, Monte Carlo simulations of fluorescence collection from emission within a turbid medium are presented. These simulations demonstrate how the collection efficiency depends on the imaging depth $z_{0,}$ the scattering MFP l_s, the absorption MFP l_a, and the origin of the emission (Figure 41 illustrates these parameters).

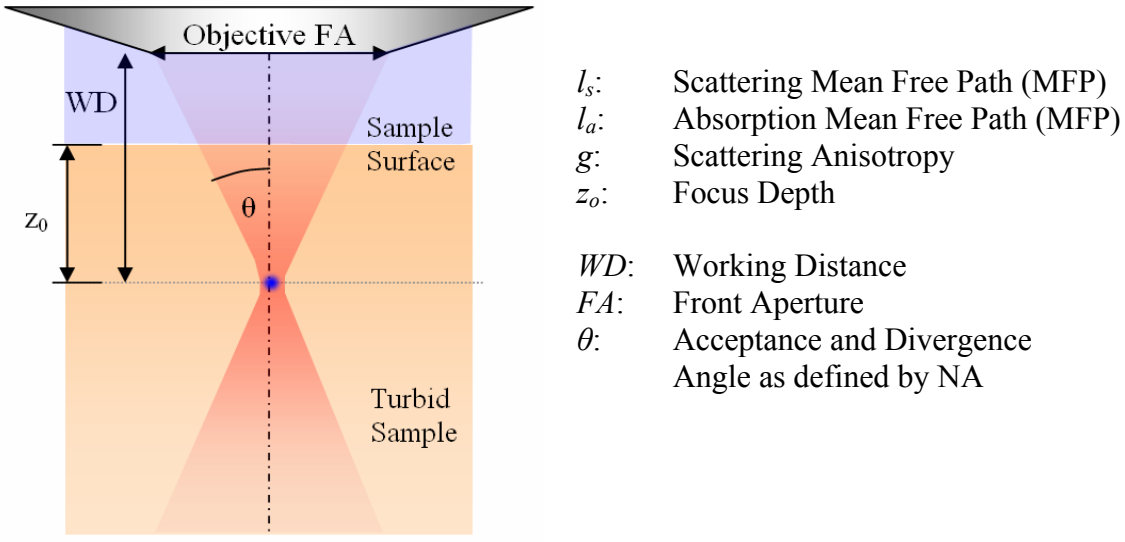

Figure 41: Schematic to explain the parameters influencing the collection efficiency from the focal point in a turbid sample.

3.5.1 Analytical considerations

In a medium without scattering and absorption, the number of photons passing through an infinitely large objective front aperture (*FA*) in any orientation will approach 50 % of the emitted photons. A finite *FA* collects a cone of light defined by the following solid angle ratio:

$$\text{Solid angle ratio} = \frac{2\pi \cdot r^2 (1-\cos\theta)}{4\pi \cdot r^2} = \frac{1}{2}(1-\cos\theta), \tag{3.5b}$$

$$\theta = \tan^{-1}\left(\frac{FA}{2 \cdot WD}\right) = \sin^{-1}\left(\frac{NA}{n}\right) \tag{3.5c}$$

The solid angle ratio increases monotonically with larger *FA* which means that a large front aperture is necessary for good collection efficiency. The 0.95 NA 20x Olympus objective has a solid angle ratio of 15 %.

A semi-infinite scattering medium with $g \neq 1$, and $l_a = 0$ will cause a long travel of emitted rays in the scattering medium until they escape. An infinite large *FA* above the scattering medium would collect 100 % instead of 50 % of the emitted light because every photon will be scattered out of the medium after infinite scattering events. A finite *FA* can also collect more than the solid angle ratio (Eq. 3.5b) from an emission point in the scattering medium because light can be scattered into the *FA*. Adding absorption to the medium will cause an exponential decay of collection with increasing distance of the emission point in the turbid medium.

These theoretical considerations explain in general how scattering increases and absorption decreases the collection from deep emission spots and corroborate the observations of the following Monte Carlo simulations.

3.5.2 The Monte Carlo Simulation Program

Monte Carlo simulations are a commonly used straight-forward method to calculate the distribution of light in turbid media [41], [32]. In this method, the computer generates random numbers which are used to calculate a new direction and a path length after each scattering event for each photon. A random path length is calculated by multiplying the

MFP with the negative natural logarithm of a random number in the interval (0, 1). This way, a random absorption path length as well as a random scattering path length is determined. The direction of the scattered light can be determined from two random numbers and the scattering anisotropy, using the approximation for Mie scattering from Henyey and Greenstein (See Equation 3.1b). Depending on the direction of the incident ray and the calculated random path length, the next position of the photon is calculated. This process is repeated until the photon escapes a specified area or exceeds the random absorption path length. In our case, a ray leaving the sample surface will be counted as collected if it hits the FA. We assume that rays will not be refracted at the surface which is a valid assumption as the refractive indices of sample and immersion fluid are matched. Simulations of a large number of photons provide results which are close to reality [42].

A Monte Carlo simulation program was developed using the Borland Delphi software package and validated with the ray tracing software: Tracepro®. With this program, we simulate photon propagation and calculate the collection efficiency for different optical parameters (Figure 42).

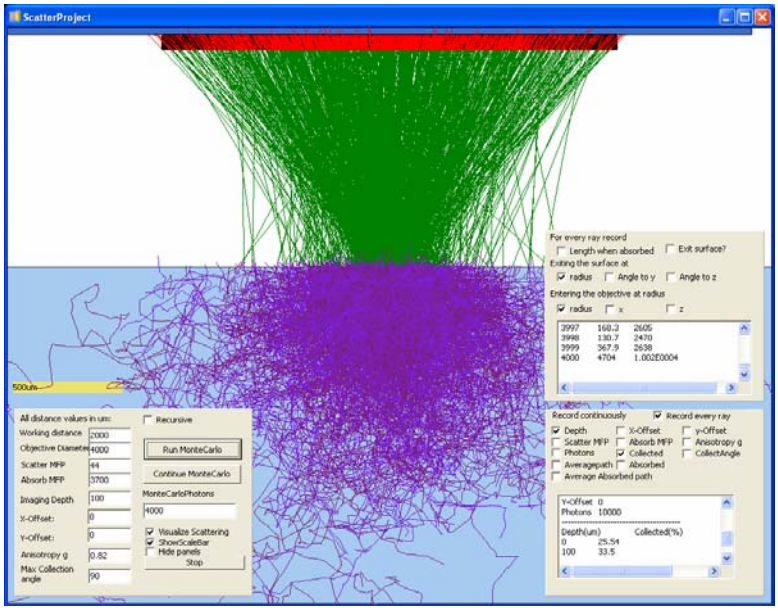

Figure 42: 'ScatterProject' – a software tool developed with Borland Delphi to simulate the collection efficiency of emission in turbid media, depending on *NA*, acceptance angle, imaging depth, l_s, l_a, g and origin.

For the parametric studies, two parameters of the objective lens were fixed: FA = 4 mm, WD = 2 mm. These parameters correspond to the most commonly used objective lens for deep tissue two-photon microscopy - the 0.95 NA 20x water immersion Olympus objective. The optical parameters of the sample are chosen to be similar to epidermis which approximately are l_s = 44 μm, l_a = 3700 μm and g = 0.82 at a wavelength of 700 nm according to Figure 27. Irregularities in the simulated curves result from the counting of random photons and can be reduced by tracing more rays. The point of emission is the focal point if not stated otherwise and all rays entering the FA are counted as collected independent on the angle of entrance. Simulations of the angle of entrance have shown that for skin tissue parameters only few rays enter the FA under steeper angles than the acceptance angle of the objective (45°), due to the distance of FA and sample surface. A complete theoretical study of tracing rays through the objective (See Figure 6) onto the PMT cathode was not in the scope of this thesis and can be examined in future simulations.

3.5.3 Dependence of Collection Efficiency on the Scattering MFP

We have simulated the collection efficiency from the focal point as a function of the imaging depth for different scattering MFP. (Figure 43)

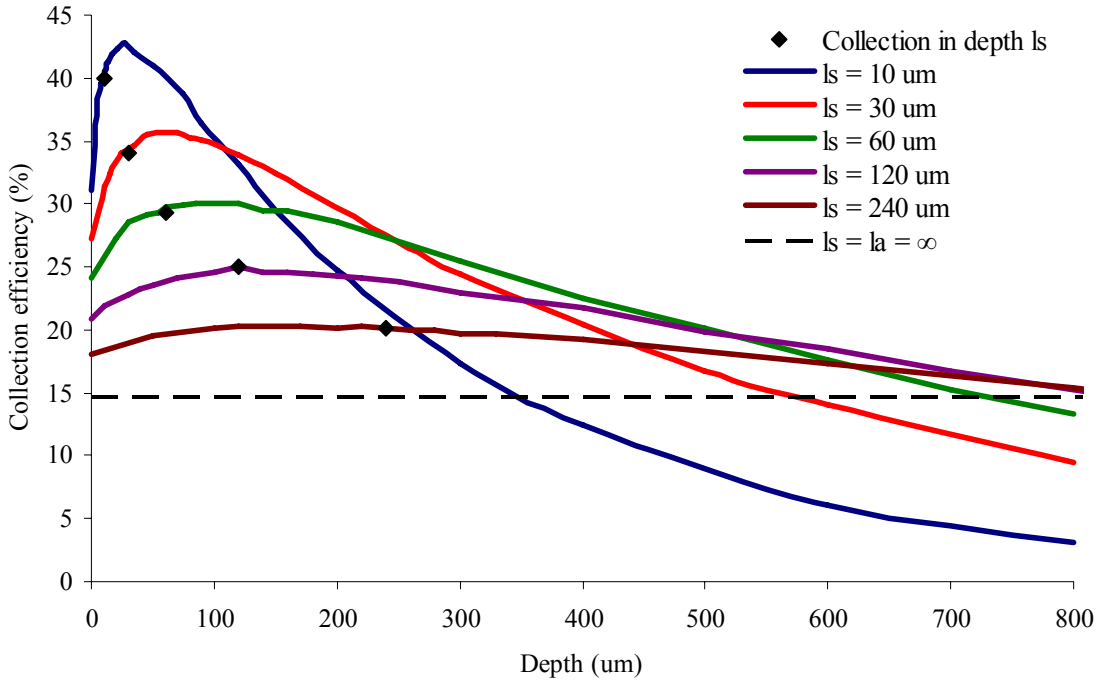

Figure 43: Monte Carlo Simulation of collection efficiency versus imaging depth (z_0) for different scattering MFP l_s. The dashed line shows the collection without scattering or absorption, which is the solid angle ratio. The black diamonds mark each line at the depth of l_s. Fixed parameters: l_a = 3700 µm, g = 0.82.

Scattering causes a notable increase in collection of emitted light from the surface because some of the backscattered light can also be collected. When the focal point moves into the turbid medium, even more photons are collected as the photons emitted to the side can eventually be scattered into the objective. At larger depths, the collection efficiency monotonously decreases which is mainly due to absorption (See Figure 44). This general behavior has also been observed by other research groups [40], [43]. The collection efficiency reaches a maximum for emission light from a depth in the range of

1-5 l_s. For short l_s, this maximum is deeper in terms of l_s and also the depth of 15 % collection is larger in terms of l_s (See black diamonds in Figure 43). Thus we can say, that scattering improves the collection efficiency from a depth down to tens of l_s, depending on other optical parameters as absorption. While scattering reduces signal generation in depth as described in 3.4, it actually helps to collect emission light at imaging depths of several l_s.

3.5.4 Dependence of Collection Efficiency on the Absorption MFP

It is in general clear that absorption decreases the collection efficiency. Nevertheless the absorption was often neglected [40] because in tissue l_a is 50 - 500 times longer than l_s. However, our simulations show that even if the absorption mean free path is much longer than the imaging depth, absorption still has the strongest effect on the collection efficiency for fluorescence from deep within turbid media (Figure 44).

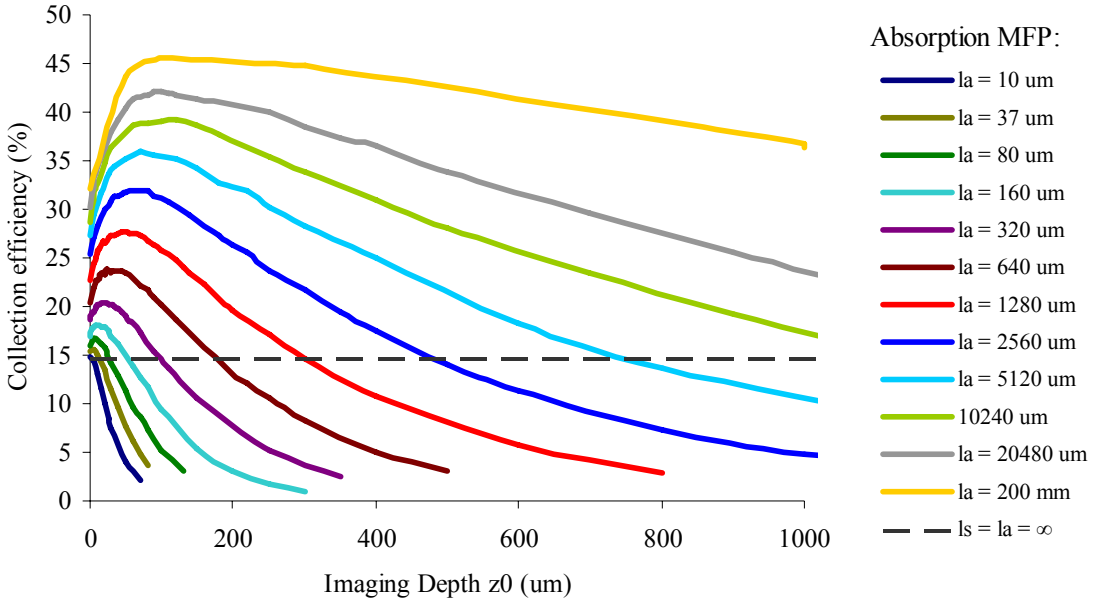

Figure 44: Monte Carlo Simulation of collection efficiency versus imaging depth (z_0) and different scattering MFP l_s. The dashed line shows the collection without scattering or absorption, which is just the solid angle ratio. Fixed parameters: l_s = 37 µm, g = 0.82.

The simulations with absorption MFP l_a up to 20 cm show the trend towards high collection efficiency without absorption. Simulations with longer l_a are time consuming because photons can be scattered up to infinity times. A logical explanation to that trend is that photons are scattered multiple times and can travel even 20 cm through the sample before entering the objective which might be just 1 mm away. Remarkable is the big difference between the collection efficiency with l_a = 2.5 mm (similar to tissue) and l_a = 200 mm (close to no absorption). This proves that the absorption can not be neglected in epithelial tissue (1 mm < l_a < 55 mm). Moreover it clarifies the importance of collecting emission light in a wavelength range with least absorption. In epidermis l_a can be up to 55 mm at a wavelength of 1100 nm compared to approximately 1 mm at 500 nm (See Figure 27). If the emission were at a wavelength of 1100 nm, the collection efficiency from emission deep in the turbid tissue would increase enormously. An optimal contrast agent should thus emit in a wavelength range with least absorption.

3.5.5 Collection Efficiency of Out-Of-Focus Fluorescence Emission

As shown in Section 3.4, in turbid media, fluorescence will be generated also in a large area near the sample surface (See Figure 40). In this section we investigate the collection efficiency from each out-of-focus point in order to allow the estimation of emission collection from focal fluorescence compared to collection from out-of-focus fluorescence. We therefore simulate fluorescence emission from points around the focal point for different imaging depths. The part of collected rays defines the collection efficiency for each of these out-of-focus points. To simplify the simulation, we observed the collection efficiency from points with a radial and an axial offset from the focal point separately. Simulations of collection from emission points with an axial offset showed that at larger imaging depths, the collection efficiency from the sample surface to the focal point increases approximately linearly with the increase of the solid angle ratio to the FA. The simulations of collection efficiency from different points with a radial offset to the focal point are displayed in Figure 45.

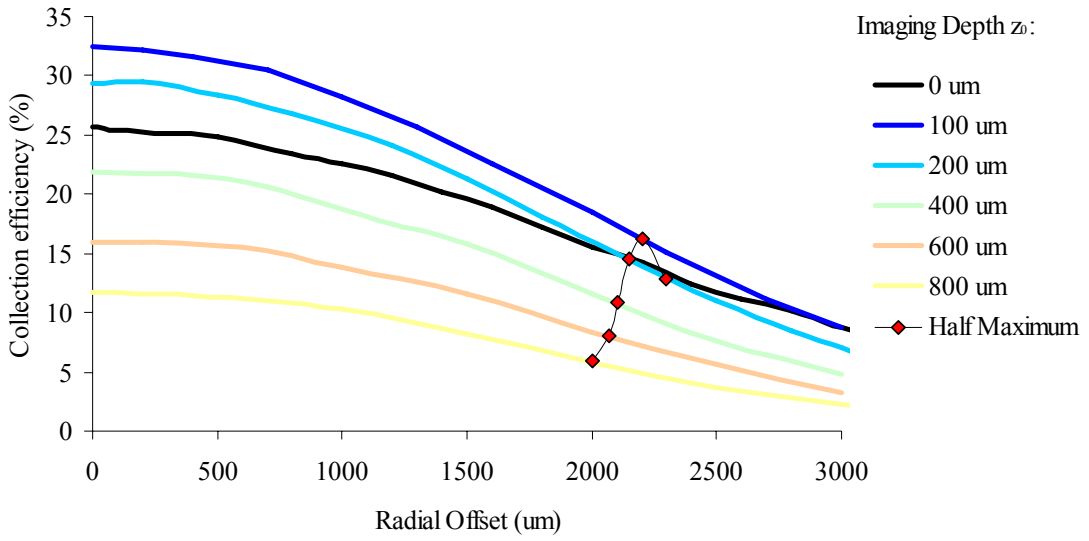

Figure 45: The collection efficiency of emission from points with a radial offset from the focal point. Note that the collection efficiency is higher at 100 µm and 200 µm imaging depth. The offset with a collection efficiency of half maximum decreases approximately linearly with imaging depth. Fixed parameters: l_s = 44 µm, l_a = 3700 µm, g = 0.82.

The decrease of the collection efficiency with a radial offset from the emission point is mainly due to the decrease of the solid angle ratio covered by the FA. The collection efficiency decrease is similar to a Gaussian curve with a FWHM of approximately the *FA*. The FWHM of this distribution decreases with imaging depth slightly due to longer path length and absorption in the turbid medium.

The measurement from Figure 45 can be combined to a two dimensional contour plot which gives a good indication of the overall collection efficiency in turbid media. The percentage of collected light for a specific imaging depth can be calculated by considering the difference of the solid angle ratio due to the distance FA to the sample surface.

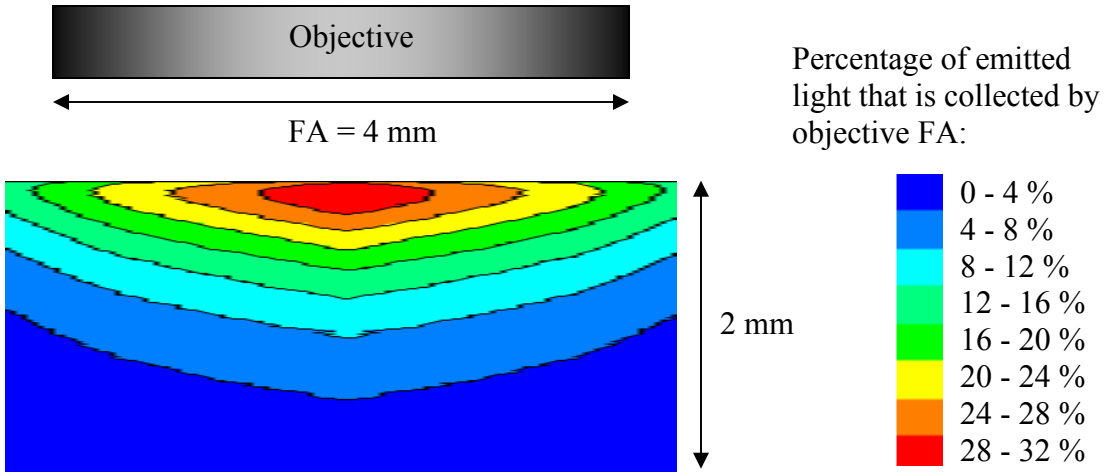

Figure 46: The distribution of the collection efficiency of equally emitting points in a turbid medium. The contour plot is generated from the data in Figure 45. Fixed parameters similar to epidermis: l_s = 44 µm, l_a = 3700 µm, g = 0.82.

3.6 Improving Imaging Depth with Contrast Agents

The calculations of fluorescence generation in section 3.4 have shown that scattering is primarily responsible for background fluorescence generation. The simulations of fluorescence collection in section 3.5 revealed that absorption is mainly responsible for a decreased collection during deep imaging. For deep imaging into turbid tissue, the ideal excitation wavelength lies in the range with least scattering and the ideal fluorescence emission would be at a wavelength with least absorption. In epidermis, the wavelength range with least scattering and thus the optimal range for excitation is from 1000 to 1400 nm while the wavelength range with least absorption and thus the optimal range for emission is from 800 to 1300 nm (See Figure 27). Autofluorescence from endogeneous fluorophores, NADH does not lie in this range. The two-photon excitation maximum of NADH is from 700 to 750 nm [34] and its emission maximum goes from 400 to 600 nm (Figure 29). To excite and emit at the optimal range for deep imaging in tissue, it is necessary to find contrast agents that can be applied in tissue for that purpose. Gold nanorods are promising contrast agents as their excitation and emission maximum can be tuned to longer wavelengths in the NIR with less scattering and less absorption, respectively.

4 Conclusion and Future Work

Two-photon microscopy has the potential to detect cancerous cells in epithelial tissue and this work examined the parameters influencing the maximum imaging depth into tissue. An upright two-photon microscope for deep imaging was built and characterized. Background fluorescence and the resulting imaging depth limit were examined and the reached imaging depth was twice as large compared to an inverted TPM previously built in the lab. The decrease of signal to background ratio, resolution and image quality of a tissue phantom was measured for different imaging depths. It was shown that imaging nanorod-labeled cells resulted in better contrast and requires less power than imaging autofluorescent cells. For further improvement of imaging depth with the TPM, it was calculated that a large area photomultiplier cathode is necessary to improve the collection efficiency.

Theoretical investigations of fluorescence generation and collection revealed that in tissue, scattering is the primary cause of high background fluorescence generation and thus limits imaging depth. Hence, a contrast agent, which can be excited at higher wavelengths with less scattering in the range of 1000 - 1400 nm, would be optimal for deep excitation into skin epidermis. Simulations of the fluorescent light collection showed that scattering improves signal collection and that absorption is the main cause of emission signal loss deep within tissue. The collection efficiency for any imaging depth was found to be maximal at a depth in the range of a few scattering lengths depending on scattering and absorption parameters. For imaging depths beyond this point, the collection efficiency decreases in an exponential manner due to absorption. For the mentioned reasons it can be inferred that the ratio of collected signal to collected background and thus the imaging depth limit can be improved by using special contrast agents, such as gold nanorods. The optimum emission maximum of contrast agents should be in the range with minimum absorption in the sample which in tissue is within 800 - 1200 nm.

Future research should include a precise calculation of the imaging depth limit by incorporating calculations of both fluorescence generation and collection. Measurements with the above described two-photon microscope should be done to prove the appropriateness of these theoretical calculations. For further imaging depth improvement with the microscope, a PMT with a larger cathode as well as sensitivity in higher wavelength ranges should be included into the setup. Sensitivity in high wavelength ranges is a step towards deep imaging with contrast agents that excite and emit at higher wavelengths with less absorption and scattering. An important investigation to evaluate the feasibility of contrast agents applied onto living human skin is to study how they penetrate skin and label cancerous cells. A contrast agent that attaches only to cancerous cells would greatly improve imaging depth, because in this case, much less background fluorescence would be generated. To turn this research into applicable technology, a two-photon endoscope that can be moved precisely around the patient's tissue, detect cancerous cells accurately and destroy them with laser pulses is under development in the lab.

5 References

[1] A. Jemal, R. Siegel, E. Ward, T Murray, J Xu, C Smigal, MJ. Thun, "Cancer statistics, 2006", CA Cancer J Clin. 56(2):106-30 (2006)

[2] V.E. Centonze and J.G. White, "Multiphoton excitation provides optical sections from deeper within scattering specimens than confocal imaging", Biophys J., 75(4): 2015–2024. (1998)

[3] W.R. Zipfel, R.M. Williams, W.W. Webb, "Nonlinear magic: multiphoton microscopy in the biosciences", Nature Biotechnology 21 (11): 1368-1376 (2003)

[4] M.C. Skala, J. M. Squirrell, K. M. Vrotsos, J. C. Eickhoff, A. Gendron-Fitzpatrick, K.W. Eliceiri and N. Ramanujam, "Multiphoton Microscopy of Endogenous Fluorescence Differentiates Normal, Precancerous, and Cancerous Squamous Epithelial Tissues", Cancer Research 65, 1180-1186, (2005)

[5] P. Theer and W. Denk, "On the fundamental imaging-depth limit in two-photon microscopy", J. Opt. Soc. Am. A, Vol. 23, (2006)

[6] N.J. Durr, T. Larson, D.K. Smith, B.A. Korgel, K. Sokolov, and A. Ben-Yakar, "Two-Photon Luminescence Imaging of Cancer Cells Using Molecularly Targeted Gold Nanorods", Nano Lett., Vol. 7, No. 4, (2007)

[7] K. Koenig, I. Riemann, "High-resolution multiphoton tomography of human skin with subcellular spatial resolution and picosecond time resolution", Journal of Biomedical Optics 8(3), 432–439 (2003)

[8] M. Göppert-Mayer, "Über Elementarakte mit zwei Quantensprüngen", Ann. Phys. (Paris) 9, 273 (1931).

[9] W. Kaiser and C.G.B. Garrett, "2-Photon Excitation in Caf2 - Eu2+", Physical Review Letters **7**(6), 229-& (1961).

[10] W. Denk, J.H. Strickler, and W.W. Webb, "2-Photon Laser Scanning Fluorescence Microscopy", Science 248 (4951), 73-76 (1990).

[11] F. Helmchen, W. Denk, "Deep tissue two-photon microscopy", Nature Methods, Vol.2 No.12 (2005)

[12] C.J. de Grauw, J.M. Vroom, H.T.M van der Voort, and H.C. Gerritsen "Imaging properties in two-photon excitation microscopy and effects of refractive-index mismatch in thick specimens", Applied Optics Vol. 38, No. 28 (1999)

[13] R. Cicchi and F.S. Pavone, "Contrast and depth enhancement in two-photon microscopy of human skin ex vivo by use of optical clearing agents", Optics Express 2337, Vol. 13, No. 7 (2005)

[14] A. Hopt and E. Neher, "Highly nonlinear photodamage in two-photon fluorescence microscopy", Biophysical Journal 80(4), 2029-2036 (2001).

[15] G.H. Patterson, D.W. Piston, "Photobleaching in Two-Photon Excitation Microscopy", Biophysical Journal Vol. 78, 2159-2162 (2000)

[16] G. McConnell, "Improving the penetration depth in multiphoton excitation laser scanning microscopy", Journal of Biomedical Optics 11(5), 054020 (2006)

[17] E. Beaurepaire, M. Oheim, J. Mertz, "Ultra-deep two-photon fluorescence excitation in turbid media", Optics Communications 188 25-29 (2001)

[18] M. Muller, J. Squier, R. Wolleschensky, U. Simon, and G. J. Brakenhoff, "Dispersion pre-compensation of 15 femtosecond optical pulses for high-numerical-aperture objectives", Journal of Microscopy-Oxford 191, 141-150 (1998).

[19] S. H. Cho, F. X. Kartner, U. Morgner, E. P. Ippen, J. G. Fujimoto, J. E. Cunningham, and W. H. Knox, "Generation of 90-nJ pulses with a 4-MHz repetition-rate Kerr-lens mode-locked Ti : Al2O3 laser operating with net positive and negative intracavity dispersion", Optics Letters 26(8), 560-562 (2001).

[20] Oheim M., Beaurepaire E. et al. "Two-photon microscopy in brain tissue: parameters influencing the imaging depth", Journal of Neuroscience Methods 112-205 (2001)

[21] J. Squier and M. Muller, "High resolution nonlinear microscopy: A review of sources and methods for achieving optimal imaging", Review of Scientific Instruments 72(7), 2855-2867 (2001).

[22] J. Mobley and T. Vo-Dinh, "Optical Properties of Tissue", Biomedical Photonics Handbook, V.-D. T., ed. CRC Press, Boca Raton, (2003).

[23] Q.-T. Nguyen, P. S. Tsai and D. Kleinfeld, “MPScope: A versatile software suite for multiphoton microscopy”, Journal of Neuroscience Methods (2006) 156:351-359

[24] D. Debarre, E. Beaurepaire, “Quantitative Characterization of Biological Liquids for Third-Harmonic Generation Microscopy”, Biophys. J.,V. 92, p.603–612 (2007)

[25] L.C. Henyey and J.L. Greenstein, “Diffuse radiation in the Galaxy”, Astrophys. J. 93, 70–83 (1941).

[26] P. Theer, “On the fundamental imaging-depth limit in two-photon microscopy”, Doctoral dissertation, University of Heidelberg, (2004)

[27] E. Salomatina, B. Jiang, J. Novak, et al., “Optical properties of normal and cancerous human skin in the visible and near-infrared spectral range”, Journal of Biomedical Optics 11 (6): Art. No. 064026 (2006)

[28] A.N. Yaroslavsky, P.C. Schulze, IV Yaroslavsky, R. Schober, F. Ulrich and H.-J. Schwarzmaier, “Optical properties of selected native and coagulated human brain tissues in vitro in the visible and near infrared spectral range”, Phys. Med. Biol. 47 p.2059–2073 (2002)

[29] P. Theer, M.T. Hasan, and W. Denk, “Two-photon imaging to a depth of 1000 μm in living brains by use of a Ti:Al2O3 regenerative amplifier”, Optics Letters, Vol. 28, Issue 12, pp. 1022-1024 (2003)

[30] H. van Staveren, C. Moes, J. van Marle, S. Prahl, and M. van Gemert, “Light scattering in Intralipid-10% in the wavelength range of 400–1100 nm”, Appl. Opt. 30, 4507–4514 (1991)

[31] ST Flock, SL Jacques, BC. Wilson, WM Star, MJC van Gemert, “Optical Properties of Intralipid: A phantom medium for light propagation studies”, Lasers in Surgery and Medicine 12:510-519, (1992)

[32] A.K. Dunn, V.P. Wallace, M. Coleno, M.W. Berns, and B.J. Tromberg, “Influence of optical properties on two-photon fluorescence imaging in turbid samples”, Applied optics Vol. 39, No. 7 /1 (2000)

[33] R. Hornung, T. Pham, K. Keefe, J. Fishkin, M. Berns, Y. Tadir, and B. Tromberg, "Quantitative near infrared spectroscopy of cervical dysplasia in vivo", Hum. Reprod. 14, 2908–2916 (1999)

[34] W.R. Zipfel, R. M. Williams, R. Christie, A. Y. Nikitin, B.T. Hyman, W.W. Webb, "Live tissue intrinsic emission microscopy using multiphoton-excited native fluorescence and second harmonic generation", Proc. Natl. Acad. Sci. U.S.A., 100, p. 7075-7080 (2003)

[35] J.A. Palero, H.S. de Bruijn, A. van der Ploeg van den Heuvel, H.J.C.M. Sterenborg, and H.C. Gerritsen, "Spectrally Resolved Multiphoton Imaging of In Vivo and Excised Mouse Skin Tissues", Biophysical Journal Volume 93 p. 992–1007 (2007)

[36] H. Wang, T.B. Huff, D.A. Zweifel, W.H., P.S. Low, A.Wei, and J. Cheng, "In vitro and in vivo two-photon luminescence imaging of single gold nanorods", Proceedings of the national academy of sciences of the united states of America 102 (44): 15752-15756 (2005)

[37] A. Bouhelier, R. Bachelot, G. Lerondel, S. Kostcheev, P. Royer, and G. P. Wiederrecht, "Surface Plasmon Characteristics of Tunable Photoluminescence in Single Gold Nanorods", Phys. Rev. Lett. 95, 267405 (2005)

[38] P. Miloni, J. Eberly, "Lasers", John Wiley & Sons, New York (1988)

[39] J.W. McLean, J.D. Freeman, and R.E. Walker, "Beam spread function with time dispersion", Applied Optics 37(21), 4701-4711 (1998)

[40] E. Beaurepaire, J. Mertz: "Epifluorescence collection in two-photon microscopy", Appl. Opt. 41, 5376-5382 (2002)

[41] B.C. Wilson and G. Adam, "A Monte Carlo model for the absorption and flux distribution of light in tissue", Med. Phys. 10, 824–830 (1983).

[42] G. Zaccanti, "Monte Carlo study of light propagation in optically thick media: point source case", Appl. Opt. 30,2031–2041 (1991).

[43] G. Ma, J.F. Delorme, P. Gallant, D.A. Boas: "Comparison of simplified Monte Carlo simulation and diffusion approximation for the fluorescence signal from phantoms with typical mouse tissue optical properties", Appl. Opt. V 46, No.10 (2007)

6 Vita

Date of Birth: April 4th 1984 in Dresden, Germany

Education

2006 - 2007	Graduate Studies of Physics, University of Texas at Austin
2003 – 2006	Studies of Physics, University of Würzburg, Germany
1996 – 2002	High-school diploma at "Martin Anderson Nexö" in Dresden

Research Projects and Work

09/2005 - 10/2005	Intern BOSCH-Central Research Stuttgart, Germany Studied UWB signals and sensors in a vehicle
02/2004 - 08/2004	ESA parabolic flight campaign, Bordeaux Spatial visualization of High-Speed processes in weightlessness
09/2003 - 10/2003	Intern, Research Center Dresden: Heavy Ion Tumor Therapy Radiation Data Processing
09/2002 - 05/2003	Civilian service at the International Center for Culture in Kassel
05/1999 - 05/2002	University of Technology in Dresden: Software development to optimize mass grinding processes

Awards and Prizes

Scholarships:	2007	▪ Fellowship at the University of Texas at Austin
	2006	▪ Full German National Merit Foundation, USA-Scholarship
		▪ Arthur Lockenvitz Memorial Endowed Scholarship in Experimental Physics
	2004	▪ Member of the e-fellows.net network
	2002	▪ Subsidy Award by E. F. Bläse
Competitions:	2002	▪ 1st Special prize by the German environment foundation at the German Youth researches competition
		▪ Winner in the Regional Youth Researches Competition
		▪ 1st Special prize by the ministry of state for work and economy
	2001	▪ Participation in the first two rounds of the International Olympiad in Physics
	2000	▪ 1st Place at German team-competition in computer science
		▪ 1st Place at German team-competition in physics
	1999	▪ Prizes at several Olympiads in mathematics

Permanent Address: Familie Holfeld
Heidemühlweg 41
01324 Dresden, Germany
benjamin.holfeld @ gmail.com